Microstructural Evolution in Additively Manufactured Fe-Cr-Ni Maraging Stainless Steel

Shahriari, Ayda; Sanjari, Mehdi; Pirgazi, Hadi; Fazeli, Fateh; Shalchi Amirkhiz, Babak; Kestens, Leo A.I.; Mohammadi, Mohsen

DOI
10.1007/s11661-022-06633-1

Publication date
2022

Document Version
Final published version

Published in
Metallurgical and Materials Transactions A: Physical Metallurgy and Materials Science

Citation (APA)
Shahriari, A., Sanjari, M., Pirgazi, H., Fazeli, F., Shalchi Amirkhiz, B., Kestens, L. A. I., & Mohammadi, M. (2022). Microstructural Evolution in Additively Manufactured Fe-Cr-Ni Maraging Stainless Steel. *Metallurgical and Materials Transactions A: Physical Metallurgy and Materials Science*, *53*(5), 1771-1792. https://doi.org/10.1007/s11661-022-06633-1

ORIGINAL RESEARCH ARTICLE

Microstructural Evolution in Additively Manufactured Fe-Cr-Ni Maraging Stainless Steel

AYDA SHAHRIARI, MEHDI SANJARI, HADI PIRGAZI, FATEH FAZELI, BABAK SHALCHI AMIRKHIZ, LEO A.I. KESTENS, and MOHSEN MOHAMMADI

In this work, the effect of heating rate on the phase transformation temperatures was investigated using dilatometry analysis. Continuous heating and isothermal holding above Ac_3 temperature on microstructural evolutions in additively manufactured (AM) parts of Fe-Cr-Ni maraging stainless steel were studied. The microstructural features developed within the heating processes were characterized employing electron backscatter diffraction and transmission electron microscopy. Austenite reversion was found to take place in two steps for the AM parts by a diffusive mechanism as well as the precipitation reactions. Although grain refinement occurred during the austenite reversion of the continuously heated samples, the microstructure showed a coarser grain size after isothermal heating. The crystallographic orientations developed after the heating processes were different from those of the initial ones implying the absence of the austenite memory effect.

https://doi.org/10.1007/s11661-022-06633-1

I. INTRODUCTION

THE requirements of modern industries for high-performance metallic structures and an advanced design along with using less material led to the emergence of additive manufacturing (AM) methods, particularly laser-powder bed fusion (L-PBF) during the last decades.[1,2] Although this fabrication method's advantages are attractive for industrial sectors, the applicability of the final products depends on the microstructure of as-printed components.[3] Post-processing techniques are required to mitigate the microstructural heterogeneities and anisotropy induced in almost all as-printed parts due to the unique heating, cooling, and solidification conditions inherited in AM process.[4–6] Among different post-processing operations, heat-treatment methods are most commonly designed to relieve the microstructural heterogeneities, as well as the residual stress.[7,8]

CX stainless steel counterparts, as a type of martensitic precipitation-hardened (PH) stainless steels, are currently intended for the L-PBF process by EOS GmbH.[9,10] CX stainless steel, similar to other low carbon precipitation hardening stainless steels, are rich in Cr and Ni and may contain other substitutional elements, such as Mo, and Al.[10] β-NiAl precipitates formed after aging treatment within a martensitic matrix of CX stainless steel similar to 13-8 Mo PH stainless steel have the main role in hardening of this alloy.[11] The solution annealing performed above Ac_3 with sequent aging at a temperature below Ac_1 is the typical heat treatment for the precipitation-hardened alloys.[12] The resultant microstructure of this low carbon martensitic stainless steel after quenching constitutes body centered cubic lath martensite.[13,14] It is also noted that reversion from martensite to austenite occurs partially in the aging process.[15,16] The reverted austenite appeared during the aging treatment has a profound effect on mechanical properties, particularly high toughness is achieved by a high amount of reverted austenite.[17] To undertake the mechanism of the martensite to austenite ($\alpha' \rightarrow \gamma$) transformation, which occurred during the aging process, some models have been proposed.[18,19] Based on the alloy composition and the applied heat treatment, two main mechanisms for reversion of austenite are proposed, including (i) a diffusional mechanism that is activated thermally and (ii) an athermal displacive or martensitic process.[20–22]

AYDA SHAHRIARI and MOHSEN MOHAMMADI are with the Marine Additive Manufacturing Centre of Excellence (MAMCE), University of New Brunswick, Fredericton E3B5A3, Canada. Contact e-mail: ashahria@unb.ca MEHDI SANJARI and BABAK SHALCHI AMIRKHIZ are with the Marine Additive Manufacturing Centre of Excellence (MAMCE), University of New Brunswick and also with the CanmetMATERIALS, Natural Resources Canada, 183 Longwood Road South, Hamilton L8P0A5, Canada. HADI PIRGAZI is with the Department of Electromechanical, Systems and Metal Engineering, Ghent University, Ghent B9052, Belgium. FATEH FAZELI is with the CanmetMATERIALS, Natural Resources Canada. LEO A. I. KESTENS is with the Department of Electromechanical, Systems and Metal Engineering, Ghent University and also with the Department of Materials Science and Engineering, Delft University of Technology, Delft 2628 CD, The Netherlands.
Manuscript submitted July 28, 2021; accepted February 10, 2022.
Article published online February 26, 2022

Diffusional mechanism of $\alpha' \rightarrow \gamma$ transformation is related to the dissolution of precipitates, which leads to a local enrichment of alloying elements acting as an austenite stabilizer.[23,24] Diffusion of Ni as the important austenite stabilizing element to dislocations and defects is supposed to result in microsegregation of this element in localized zones, leading to the formation of reverted austenite.[25]

Furthermore, a shear mechanism assisted by a diffusional process is suggested for the formation of lath-like austenite in high Ni maraging steels.[26] However, to the author's best knowledge, there is yet a lack of investigation about the mechanism of the $\alpha' \rightarrow \gamma$ transformation in CX stainless steel fabricated by L-PBF technique. Although some researchers have focused their interests recently on revealing the microstructural features, the mechanical properties, and the relationship between the heat treatments and the microstructure of additively manufactured martensitic precipitation hardened stainless steels,[27–30] there is a lack of information concerning the effect of unique microstructure developed by L-PBF technique on austenite reversion mechanism in these steels. This study focuses to investigate the microstructural features developed within continuous and isothermal heating, particularly the reverse transformation of martensite to austenite in CX stainless steel fabricated by L-PBF technique. To achieve a deeper conception of microstructural evolution during the heating processes, dilatometry tests, as well as transmission electron microscopy (TEM) and electron backscatter diffraction (EBSD) techniques were conducted. In addition, based on experimental results and simulations, the mechanisms involved in the $\alpha' \rightarrow \gamma$ transformation are discussed.

II. EXPERIMENTAL METHODS

A. *Material*

In this study, CX stainless steel (SS CX) test samples were fabricated using an EOS M290 metal 3D printer. The gas-atomized powder of SS CX was acquired from EOS Company; the chemical composition of this powder is shown in Table I. The rod-shaped samples with dimensions φ 12 mm × 120 mm were produced in the horizontal and vertical directions using the stripe scanning method with 67° rotation between consecutive layers, as shown in Figure 1. The samples were fabricated under an argon purging atmosphere (99.9 pct) where the laser was operated at a power of 258.7 W with a scanning speed of 1066.7 mm/s, hatching distance of 100 μm, and layer thickness of 30 μm.

The horizontal build direction means that the longitudinal axis of the rod-shaped samples was parallel to the build platform (X–Y plane), and the vertical samples are those with their longitudinal axis parallel to the Z-direction, as shown in Figure 1(a). Three types of heating experiments were connected: (a) dilatometry measurements to determine phase transformation temperatures, (b) continuous heating up to 600 °C, 800 °C, and 1100 °C temperatures and subsequent gas quenching to room temperature, (c) isothermal heating including: (I) austenitization annealing at 900 °C with changing soaking time followed by quenching, and (II) austenitization annealing at 900 °C with subsequent aging. All types of experiments are described in detail below.

B. *Dilatometry Measurements*

Dilatometry tests were conducted to define the phase transformation temperatures of the samples as a function of heating rate using a Bahr DIL 805 deformation dilatometer (Hüllhorst, Germany) with programmable heating-holding–cooling cycles. For these experiments, vertical specimens with 6.67 mm diameter and 10 mm height were cut from the as-built material (Figure 1(b)). First, a pretreatment was conducted, that included heating the samples at 0.5 °C/s to 1100 °C and soak for 30 minutes, followed by argon gas quenching. Subsequently, specimens were heated up to 1100 °C with different heating rates (0.5, 1, 5, and 20 °C/s) and holding time equal to 10 minutes. The material was then helium gas cooled to room temperature. The sample contraction within heating cycles was recorded to grasp dilatometry results. To determine the start and finish phase transformations temperatures, the tangent intersection method was applied.[31]

C. *Continuous Heating*

For continuous heating, the rod-shaped vertical samples of 6.67 mm diameter and 10 mm height were heated at a slow rate of 0.5 °C/s up to 600 °C, 800 °C followed by helium gas quenching to room temperature in the dilatometer. These processed samples to 600 °C and 800 °C are referred to as CH_1, CH_2, respectively. Also, one of the samples referred to as CH_3 was heated at 0.5 °C/s to 1100 °C and held for 30 minutes with subsequent helium gas quenching to room temperature. Pretreatment was performed on CH_1 and CH_2 samples consisting of heating at 0.5 °C/s to 1100 °C and soaking for 30 minutes, followed by helium gas quench.

D. *Isothermal Heating*

The horizontal samples were also cut from plates parallel to the build direction (Y–Z planes) (shown in Figure 1(c)) and located in an infrared heating furnace under a vacuum atmosphere (about 0.1 Pa). Two different heat treatment processes were connected as follows:

(i) Samples were subjected to austenitization annealing at 900 °C and isothermally soaked for different periods of 10, 20, and 60 minutes followed by quenching in air. The samples for this step are labelled as IH_1, IH_2, and IH_3, respectively.
(ii) Some of the IH_3 samples were subsequently aged at 530 °C for 3 hours, followed by rapid air cooling to room temperature and indicated as H_3G.

Table I. Chemical Composition of the SS CX Powder

	Cr	Ni	Mo	Mn	Si	Al	C	Fe
wt pct	12.48-13	8.4-10	1.46-1.7	0.37-0.4	0.12-0.4	1.32-2	0.05	bal.

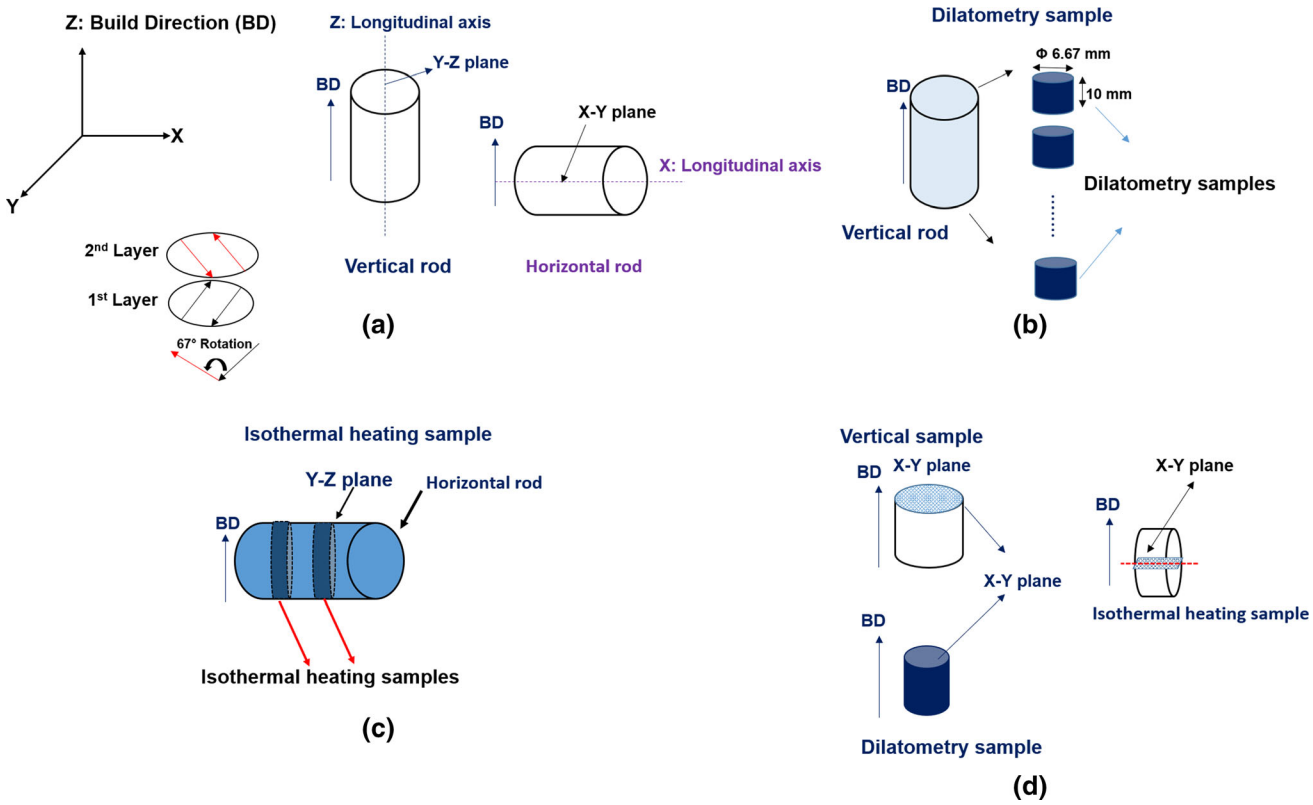

Fig. 1—Schemes of (*a*) the build orientations and laser scanning direction for the vertical and horizontal rods, (*b*) dilatometry samples cut out from vertical rods, (*c*) isothermal heating samples cut out from horizontal rods, and (*d*) planes of vertical, isothermal and dilatometry samples were selected for the microstructural characterization.

Nomination of samples and a scheme of all applied thermal cycles are shown in Table II and Figure 2 Also, the as-built samples were considered for comparison with the heat-treated specimens.

E. *Microstructural Characterization*

Microstructural analysis was carried out on both continuous heating (CH_1, CH_2, and CH_3) and isothermal heating (IH_1, IH_2, IH_3, and H_3G) specimens. TEM and electron-backscattered diffraction (EBSD) techniques were employed to analyze the samples' microstructure. Lift-out technique was used to prepare samples for the TEM investigations using a focused ion beam (FIB) system (FEI Helios NanoLab 650 dual-beam). An FEI Tecnai Osiris TEM operating at an accelerating voltage of 200 kV and equipped with a Super-X silicon drift detector (SDD) energy-dispersive X-ray spectroscopy system (EDXS) was used for TEM studies. For EBSD analyses, specimens were ground and polished using a Tegramin-30 Struers auto-grinder/polisher. EBSD observations were conducted with a HR-FEGSEM (high-resolution field emission gun scanning electron microscope) of type FEI QUANTA 450 equipped with TSL-OIM software. EBSD characterizations were also performed in the plane perpendicular to the built direction for both vertical and horizontal specimens, as shown in Figure 1(d). The measurement areas of ~ 0.25 mm^2 were scanned with a step size of 0. 5 μm with a sample tilt of 70 deg. To characterize the reversed austenite, X-ray diffraction (XRD) peak profiles of all samples were recorded on the polished segments in a Siemens D5000 instrument equipped with a 40 kV Mo-K_α source.

III. RESULTS

A. *Dilatometric Measurements*

Figures 3(a) through (c) show dilatometry curves recorded during the continuous heating of the L-PBF samples fabricated in the vertical built direction. Figure 3(a) depicts the ratio of change in the length

(ΔL) to the original length (L_0) versus temperature at different heating rates of 0.5, 1, 5, and 20 °C/s. The start (P_s) and finish (P_f) precipitate transformation temperatures, as well as the austenite initiation (As_1), and austenite finish (Af_1) temperatures for the first step and austenite start (As_2) and austenite finish (Af_2) temperatures for the second step of the martensite to austenite transformation ($\alpha' \rightarrow \gamma$) are indicated on the plot. As seen from Figure 3(a), the martensite to austenite shows two steps at heating rates up to 5 °C/s, and there is only one step of $\alpha' \rightarrow \gamma$ transformation at the heating rate of 20 °C/s. It is observed that both the precipitation and the $\alpha' \rightarrow \gamma$ transformation begin at higher temperatures as the rate of heating increases and no precipitation stage is observed during heating rate of 20 °C/s. The trace of heating rate on the $\alpha' \rightarrow \gamma$ the transformation is detected more obviously in the derivatives of the $(\frac{\Delta L}{L_0})$ versus temperature as shown in Figures 3(b) and (c). The tangent intersection principle rule was applied to the derivative plots (Figure 3(c)) at four heating rates planed in this study to calculate the transformation temperatures, as shown schematically in Figure 3(b). The locations of P_s, P_f, As_1, Af_1, As_2, Af_2 are marked with the arrows in Figure 3(c). Besides, a small change in slope or spike in the curves as marked with red arrows in Figure 3(c) could be related to the ferromagnetic to paramagnetic transformation of α'.[32] As indicated in Figure 3(c), while heating rates increase, the peaks related to the precipitation transformation, the first and second steps of the $\alpha' \rightarrow \gamma$ transformations shift up to higher temperatures.

Moreover, the relative extents of $(1/L_0)\ dL/dT$, which determine the transformation rate during the continuous heating, diminishes with the increasing heating rate; this is especially in the area related to the precipitation reactions and the second step of $\alpha' \rightarrow \gamma$ transformation. The location of the $\gamma/\alpha' + \gamma$ phase boundaries is also estimated from the equilibrium phase diagram of a Fe-13 pct Cr-Ni alloy (Figure 3(d)).

Thermo-Calc software was used to calculate the isopleth section of the Fe-13 pct Cr-Ni phase diagram. A comparison between the $\alpha' \rightarrow \gamma$ transformation temperatures calculated from dilatometry diagrams (shown in Table III) and $\gamma/\alpha + \gamma$ phase boundaries temperatures (Ae_3) calculated by Thermo-Calc indicates that the Af_1 temperatures of the continuously heated samples are higher than Ae_3 (between 650 °C and 662 °C). Therefore, the $\alpha' \rightarrow \gamma$ transformation is thermodynamically possible to occur according to a diffusional mechanism under paraequilibrium.[33] The increasing trends in transformation temperatures observed from Figures 3(a) and (c) can also postulate a mechanism involving long-range diffusion of alloying elements. The heating rate's sensitivity is more pronounced in a long-range diffusion mechanism than the short-range diffusion or shear mechanism based on relative atomic motion smaller than the interatomic spacing.[34]

Figure 4 shows the dependency of transformation temperatures on heating rates on the semi-log plot. As seen from Figure 4, there is a linear dependency of Ps and As_1 temperatures with the heating rate, which can be attributed to the diffusion-controlled mechanism.[35] A similar trend was reported from the kinetical model proposed to the phase transformation under a diffusional mechanism.[35] However, the value of *R*-squared (R^2) of the line fitted to As_2 temperatures versus heating rates was about 0.46, which shows there is a higher deviation of linearity behavior compared with the As_1 temperature. This deviation could be related to some uncertainty in the calculation of transformation temperatures using a dilatometer. The uncertainty could be associated with the acquisition of data during a single dilatometry test, and its subsequent analysis to obtain the start and finish temperatures using the gradient method.[36]

B. *Phase Fraction of Austenite*

X-ray diffraction experiments were conducted to estimate the amount of austenite that has remained after the L-PBF and the heat-treating processes. Figure 5 displays the SS CX samples' XRD patterns fabricated by the L-PBF method either in vertical or horizontal built directions and after different heat treatments.

Table IV tabulates the phase fraction of retained/reversed austenite (RA) in all samples with different heat treatment processes. The as-built vertical samples ($A\text{-}S_1$) as well as the continuously heated samples up to 600 °C (CH_1), and 1100 °C (CH_3), exhibited a single structure of the body-centered cubic (α'-martensite). However, a few diffraction peaks related to γ-austenite phase have been detected in XRD-patterns of the continuous heated sample up to 800 °C (CH_2). Based on XRD results, the as-built horizontal sample ($A\text{-}S_2$) and the austenitization annealing-aged sample (H_3G) reveal the detectable diffraction peaks of the γ phase. However, the diffraction lines belonging to γ phase are not detected in the XRD patterns of the other isothermal heating samples, which were annealed at 900 °C at different soaking times of 10, 20 and 60 minutes. The volume fractions of austenite (V_γ) were quantified using the Direct Comparison Method, which was proposed by Cullity.[37] The integrated intensity of the (200) and (211) peaks of the BCC phase shown as I_α^{200} and I_α^{211}, respectively, as well as I_γ^{220} and I_γ^{311} as the integrated intensity of the (220) and (311) peaks of the FCC phase are used in this method according to Eq. [1]:

$$V_\gamma = \frac{\frac{I_\gamma^{220}}{1.42I_\alpha^{200}+I_\gamma^{220}} + \frac{I_\gamma^{220}}{0.711I_\alpha^{211}+I_\gamma^{220}} + \frac{I_\gamma^{311}}{1.62I_\alpha^{200}+I_\gamma^{311}} + \frac{I_\gamma^{311}}{0.81I_\alpha^{211}+I_\gamma^{311}}}{4} \quad [1]$$

The results reveal that the as-built horizontal sample, as well as the continuous heated sample up to 800 °C and the austenitization annealing-aged specimen, contained more austenite in comparison with those of the rest. The volume fraction of austenite in the rest of the specimens was negligible. In addition, due to the limited detection accuracy of the XRD tests, the volume fraction of less than 3 vol pct cannot be detected. Re-heating to the austenite phase during the isothermal

Table II. Heat Treatment Processes and Nomination of Samples

Process	Pre-treatment			Build Direction					Sample
	Temperature (°C)/ Heating Rate (°C/s)	Soaking Time (min)	Quenching		Temperature (°C)/ Heating Rate (°C/s)	Soaking Time (min)	Quenching	Aging, Temperature (°C)/Time (min)	
No process (as-built)	—	—		vertical	—	—			$A\text{-}S_1$
Continuous heating	1100/0.5	30	RT	vertical	600/0.5	0.5	RT		CH_1
Continuous heating	1100/0.5	30	RT	vertical	800/0.5	0.5	RT		CH_2
Continuous heating	—	—		vertical	1100/0.5	30	RT		CH_3
No process (as-built)	—	—		horizontal	—	—	—		$A\text{-}S_2$
Austenitization annealing	—	—		horizontal	900	10	RT		IH_1
Austenitization annealing	—	—		horizontal	900	20	RT		IH_2
Austenitization annealing	—	—		horizontal	900	60	RT		IH_3
Austenitization annealing & aging	—	—		horizontal	900	60	RT	530/180	H_3G

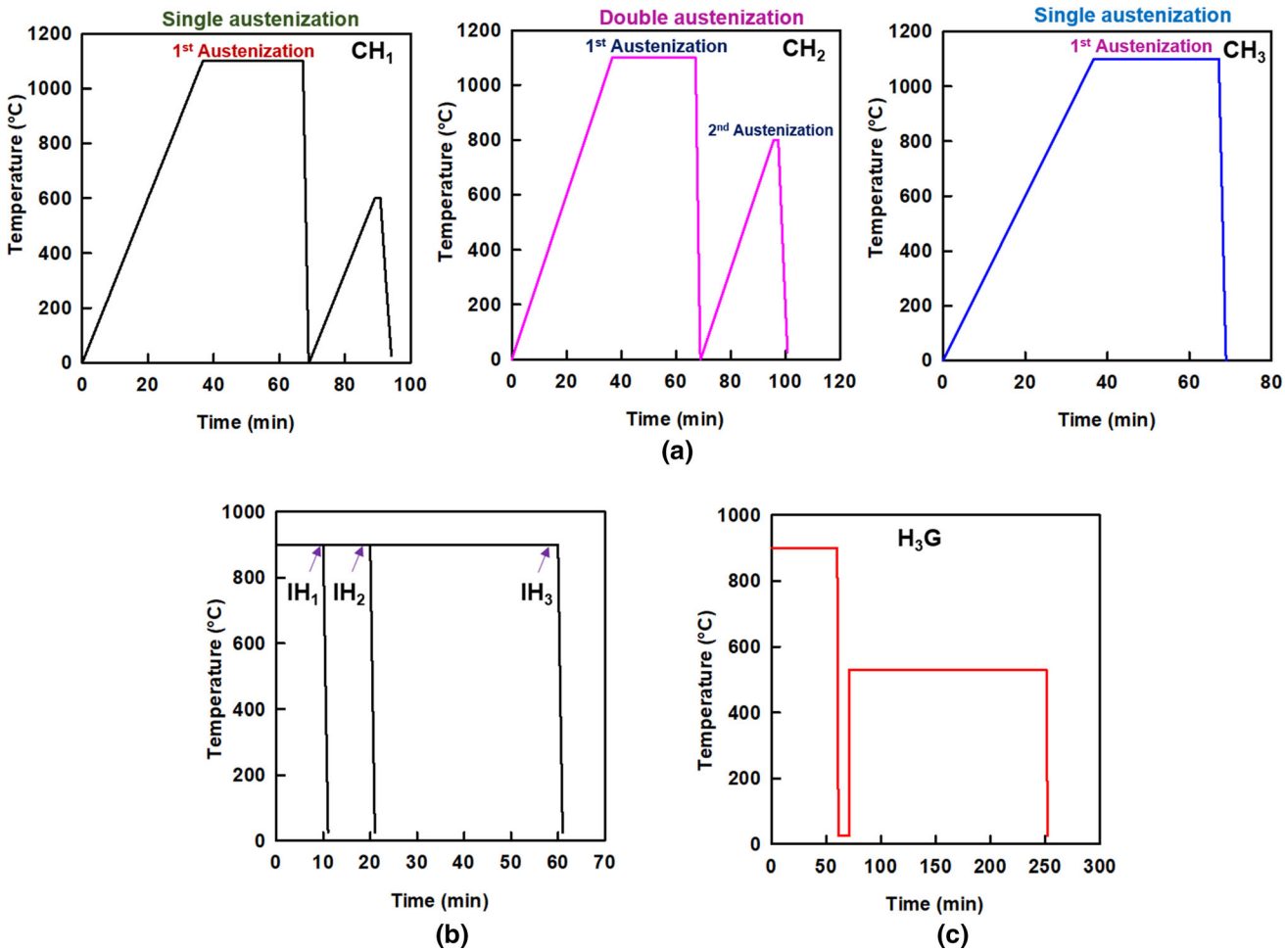

Fig. 2—Schemes of the different heat treatment processes connected to the SS CX samples, including (*a*): continuous heating; (*b*): Austenitization annealing; and (*c*): Austenitization annealing and the aging process.

heating can provide a homogenization condition. Accordingly, the diffusion of the alloying elements such as Ni in the form of microsegregations formed during the solidification process is possible.[38,39] Subsequently, the austenite stability could reduce after quenching, which results in negligible austenite content in the IH_1, IH_2, and IH_3 samples. Reheating to the austenite phase during the isothermal heating process, could provide a proper condition for diffusion of alloying elements resulting in decomposition of retained austenite and homogeneous distribution of segregated alloying elements. Therefore, the austenite content of the L-PBF sample reduces after subsequent isothermal heating. The re-heating and cooling during the L-PBF process could also induce in-situ diffusion processes similar to the tempering procedure in which austenite retention is possible.[3,40] Accordingly, a large amount of RA (about 12 pct) revealed in the as-built sample ($A\text{-}S_2$) can correspond to multi- heating and cooling cycles within the L-PBF process. The austenite content of the H_3G sample is about 4 pct. The XRD results showed that the volume fraction of RA after the austenitization annealing is negligible (volume fraction of γ in IH_1, IH_2 and IH_3 samples). Thus, it is rational to derive that the entire austenite detected for the H_3G sample is related to the reverted austenite. The equilibrium phase fraction calculations were performed using JMatPro software for chemical composition in the range of CX stainless steel, which consists of 0.05C-12.48 Cr-8.4 Ni-1.46 Mo-0.37 Mn-0.12 Si-1.32 Al (shown in Figure 6). The phase fraction estimations confirmed that aging at 530 °C provides the proper condition for austenite's reversion. Although the CH_1 and CH_3 samples contain no austenite after quenching, CH_2 shows the highest volume fraction of austenite phase among them, which is about 5 pct. A postulate can be the dissolution of the NiAl precipitates during the continuous heating of the CH_2 sample, which affects $\alpha' \rightarrow \gamma$ transformations as well as the austenite stability after quenching.[41,42] According to Figure 6, dissolution of NiAl precipitates is possible at the temperature at which the CH_2 sample is heated up resulting in a localized enriched region with Ni that can be retained as austenite upon cooling to room temperature. The negligible content of austenite in CH_1 sample can be associated with the insufficient time for the diffusion of the austenite stabilizer elements such as Ni. In contrast to CH_1, the CH_3 sample probably has

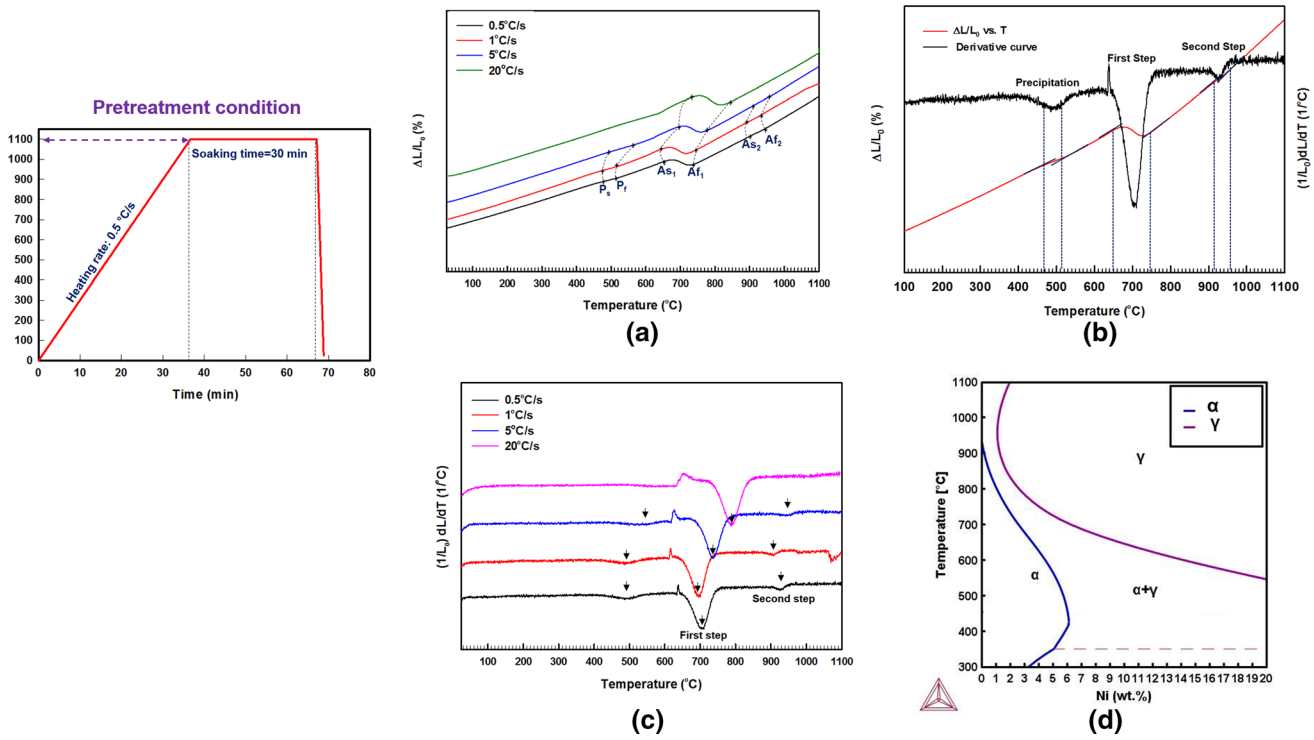

Fig. 3—(*a*) Dilatometry curves of four different heating rates, and (*b*) Schematic diagram of an experimental dilatometry plot (measured at 0.5 °C/s) to estimate transformation temperatures via tangent intersection principle and also its derivative, $(1/L_0)\,dL/dT$ vs. T, (*c*) $(1/L_0)\,dL/dT$ vs. T for different heating rates, and (*d*) Pseudobinary phase diagram for Fe-13 pct Cr-Ni, variable 0-20 wt pct Ni. (Pre-treatment condition which is heating at the rate of 0.5 °C/s to 1100 °C and 30 minutes soaking with gas quenching to room temperature, is inserted to this figure).

Table III. Comparison of the Transformation Temperatures for the Continuously Heated Samples

Heating Rate (°C/s)	P_s (°C)	P_f (°C)	As_1 (°C)	Af_1 (°C)	As_2 (°C)	Af_2 (°C)	Ae_3 (°C)
0.5	480	525	650	750	920	960	650-662
1	480	530	650	750	910	950	650-662
5	490	570	700	770	930	970	650-662
20	—	—	740	860	—	—	650-662

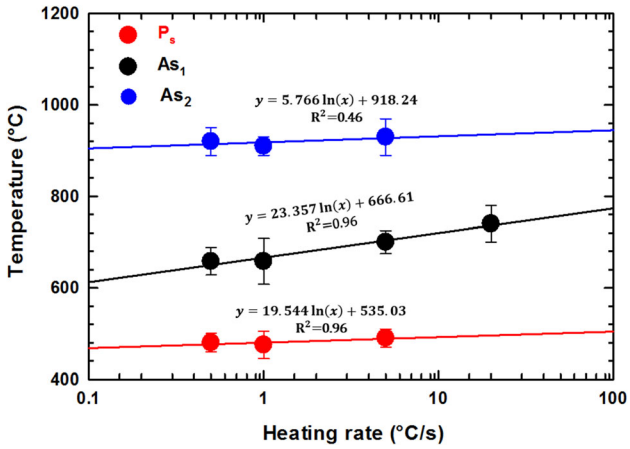

Fig. 4—Effect of heating rates on the transformation temperatures.

found a sufficient time to undergo homogenized and complete the $\alpha' \rightarrow \gamma$ transformation at 1100 °C.[40]

C. *Microstructure Changes During the Continuous Heating*

Figure 7 presents the EBSD measurements of the SS CX alloy produced by the L-PBF method (L-PBF SS CX) in as-built condition and after continuous heating up to different temperatures of 600 °C, 800 °C, and 1100 °C and subsequent rapid cooling. To compare the crystal orientations, inverse pole figures (Z-IPF) color coding of the martensitic structures with a misorientation angle >15 deg are accounted and displayed in Figures 7(a) through (d). Furthermore, a reconstruction of the parent austenite grain (PAG) structure from the original martensitic microstructures are calculated based on the approach developed by Gomes. *et al.*[43] and shown in Figures 7(e) through (h) to evaluate the changes in crystallographic orientations after continuous heating to different temperatures. The $\{001\}_\alpha$ pole figures taken from the martensitic structures are also shown in Figures 7(i) through (l).

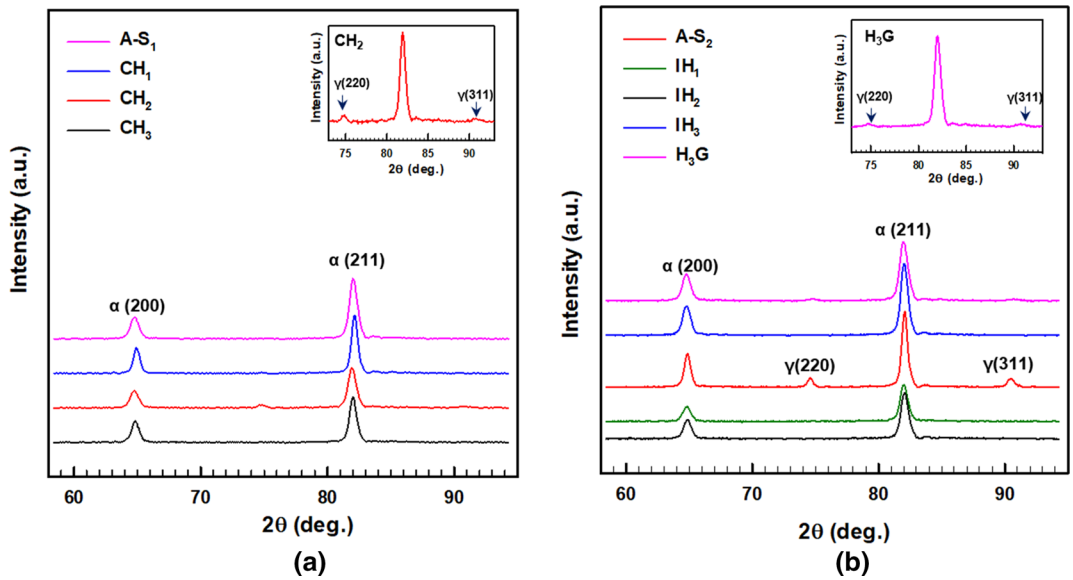

Fig. 5—XRD patterns of heat-treated samples (*a*) continuous heating samples, and (*b*) isothermal heating specimens.

Table IV. The Volume Fraction of the Austenite in the As-Built and Heat-Treated SS CX Samples (Obtained via XRD)

Sample	The Volume Fraction of Austenite (Pct)
$A\text{-}S_1$	—
CH_1	—
CH_2	5
CH_3	—
$A\text{-}S_2$	12
IH_1	—
IH_2	—
IH_3	—
H_3G	4

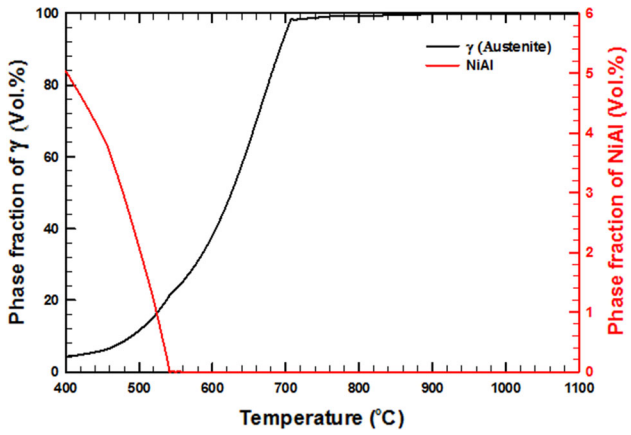

Fig. 6—Equilibrium phase fractions of the austenite and NiAl precipitates for the chemical composition of 0.05C-12.48 Cr-8.4 Ni-1.46 Mo-0.37 Mn-0.12 Si-1.32 Al-75.8 Fe.

The lath martensite structures comprising of packets and blocks as substructures of lath martensite are observed from all IPF maps shown in Figures 7(a) through (d). It seems that the martensitic structure of the continuous heat-treated samples, as well as their corresponding PAGs, give rise to more equiaxed grain structure compared to that of the as-built specimen as shown in Figures 7(a) through (d) and (e) through (h). Furthermore, a comparison between the $\{001\}_\alpha$ pole of the as-built and continuous heated samples shows the accumulation of different crystal orientations of the martensite (variants) is higher in the as-built sample. The higher accumulation of $\langle 100 \rangle$ planes oriented in specific directions in the as-built sample could be explained based on solidification patterns, which depend on the local temperature field in the melt-pools and affect the grain growth orientation.[44] Also, the distribution and intensity of variants after the continuous heating have deviated from the as-built sample, which can be attributed to some extent to recovery and recrystallization occurring during the continuous heating.[45,46] Furthermore, the crystallographic orientation between lath martensite and PAG in martensitic low carbon steels is mostly stated to be near the Kurdjumov-Sachs (K-S) orientation relationship (OR), which claims the close-packed planes and close-packed directions of the parent and daughter phase are parallel, i.e. $\{111\}_\gamma \| \{011\}_{\alpha'}$ and $\langle 011 \rangle_\gamma \| \langle 111 \rangle_{\alpha'}$.[47] This OR results in 24 possible variants of martensite crystals out of a single prior austenite crystal orientation (PAG) depicting a characteristic pattern in the {001} pole figure.[48,49] The K-S orientation was also detected in low carbon ferritic-martensitic steel fabricated by AM method.[50] Accordingly, the $\{001\}_\alpha$ pole figure taken from single parent austenite grain of the as-built sample (Figure 8) shows the traces of the K-S OR between the parent austenite and martensite laths. However, in addition to K-S orientation, traces of Nishiyama–Wassermann

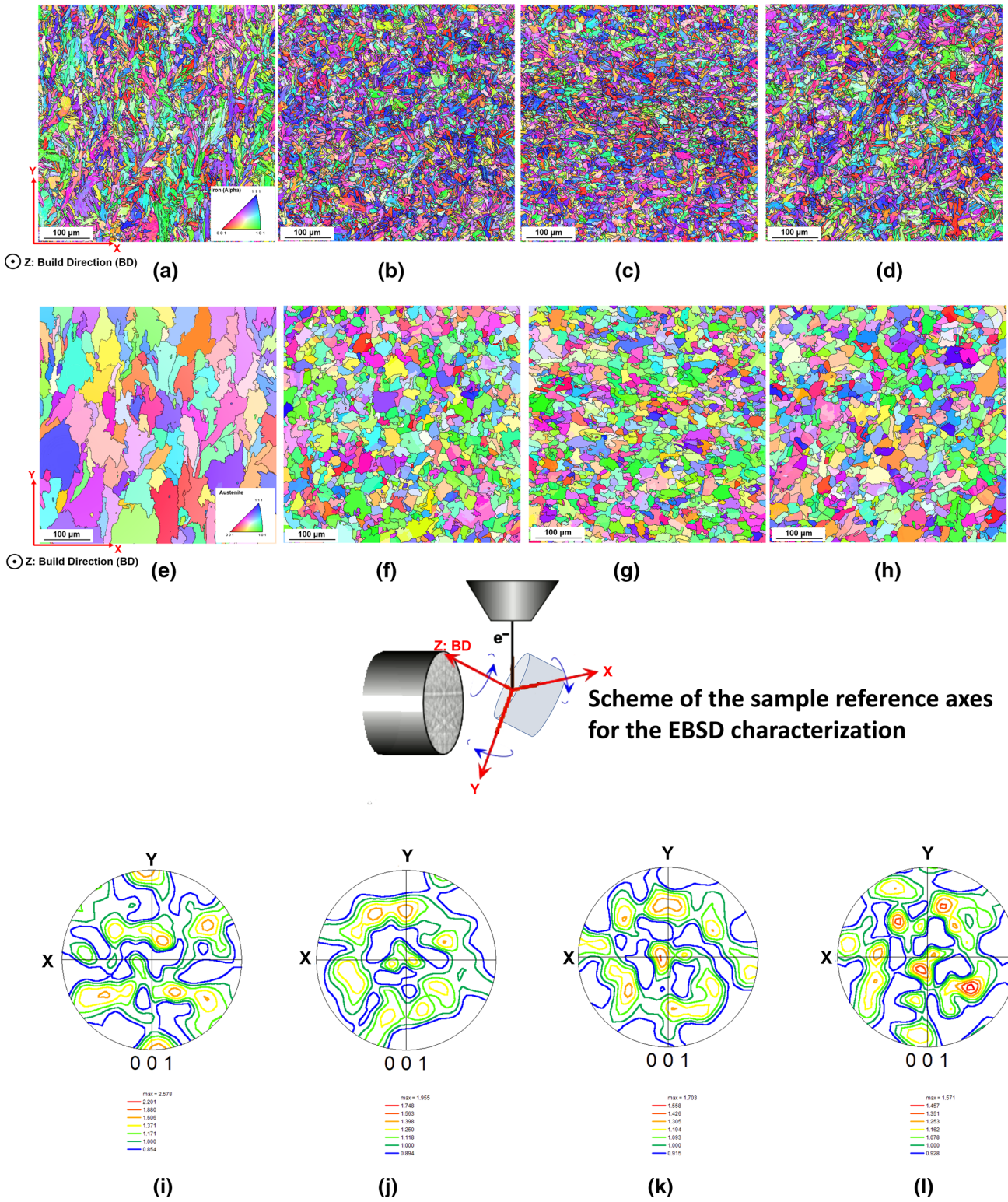

Fig. 7—EBSD measurements of martensitic microstructure of the continuous heat-treated samples; (*a*), (*e*), (*i*): A-S_1, (*b*), (*f*), (*j*): CH_1, (*c*), (*g*), (*k*): CH_2, (*d*), (*h*), (*l*): CH_3, (a) through (d): EBSD orientation map (Z-IPF) maps, (e) through (h): Reconstructed prior austenite grains (PAG) from the martensitic microstructures, (i) through (l): Corresponding $\{001\}_\alpha$ pole figures.

(N–W) OR were also observed in the previous work of our group on CX stainless steel fabricated by the L-PBF method.[51]

Figure 9 shows grain-shaped aspect ratio (GAR) maps and the corresponding grain size, plotted versus area fraction for the as-built and continuously heated samples. The GAR maps were analyzed to achieve a

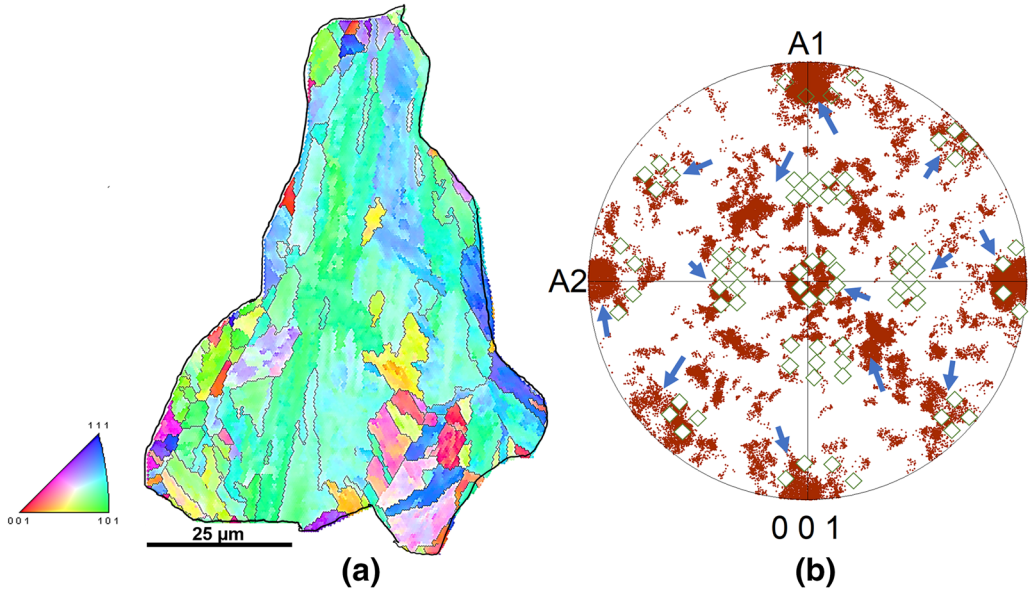

Fig. 8—(*a*) Z-IPF color coding of one exemplary prior austenite grain of the as-built sample (A-S_1), and (*b*) a $\{001\}_\alpha$ pole figure with reflections of martensite of the exemplary prior austenite grain. (Blue arrows show positions of near K-S variants in a single PAG, and green diamonds show the location of 24 ideal variants of K-S) (Color figure online).

vision of morphological changes in the martensite substructure. The GAR maps were achieved by assuming martensite blocks as bcc grains defined by high angle grain boundaries (HAGBs), having a misorientation larger than 15 deg. The block morphology was studied based on the $\frac{c}{a}$ ratio, in which "*a*" is equal to the block's length and "*c*" is equal to the block width, presuming the lath length equal to the block length, and each block is composed of several laths. Three different ranges of $\frac{c}{a}$ ratio are shown in three different colors, as shown in Figure 9. The martensitic structures resulting from the continuously heated samples exhibit the higher fractions of the blocks with the $\frac{c}{a}$ higher than 0.33 in comparison with those of the as-built sample. The morphology and grain size results indicated that the continuous heating pushes the morphology of the martensitic blocks to a more equiaxed shape. Moreover, as shown in Figure 9, asymmetric grain size distribution is found for the as-built sample with a high average grain size, whereas the distribution of grain size for the continuously heated samples is more symmetric with smaller average grain sizes than those in the as-built condition.

The grain size distribution of the reconstructed PAGs of the as-built and CH samples are shown in Figure 10(a). The main peak of the grain size distribution plots of the continuously heated samples shifts to the left, as the mean peaks lie below 30 μm, whereas the peaks of the as-built sample shift to higher values. These results as well as the morphology and grain size analyses of the martensitic structures (Figure 9) confirm the martensite blocks in continuously heated samples have formed from more equiaxed and smaller parent austenite grains in comparison with those of the as-built sample due to either a single austenitization (CH_1 and CH_3) or double austenitization cycle (CH_2). The double austenitization of CH_2 and single austenitization of CH_1 and CH_3 upon heating at rate of 0.5 °C/s could result in a new formation of austenite structure from the initial martensite structure. Furthermore, comparing the shape of the PAGs of the as-built and those of continuously heated samples (Figures 7(e) through (f)) as well as the analyses of the PAGs' grain size distributions shown in Figure 10(a) do not reveal the identical grain structure with the PAGs of the as-built sample implying there is no direct evidence of the austenite memory effects.[52,53]

The kernel average misorientation distributions (KAM) of the as-built and CH samples are shown and compared in Figure 10(b). The kernel average misorientation (KAM) is a measure of local grain misorientation, which can evaluate a density of geometrically necessary dislocations.[54] By comparing the samples, the KAM after continuous heating to 600 °C and 1100 °C shifts to larger misorientation angles so that the average values of KAM increase from 1.3 deg measured for the initial one (A-S_1) to about 2 deg for CH_1 and CH_3 samples. However, a slight shift is observed between the KAM of the as-built sample and that of the continuously heated sample to 800 °C (CH_2). These results also indicate that the dislocation density in the continuously heated samples to 600 °C and 1100 °C is higher than that of the as-built sample. The increase in the KAM value of the CH_3 sample can be associated with the austenite reversion, which occurred during heating up to 1100 °C and created a finer structure compared with the grain structure of the initial PAGs related to the as-built sample. Eventually, the new austenite grains undergo a martensitic transformation, which is accompanied by a high density of dislocations.[55] After re-heating to 600 °C, the KAM value is lower than that of the CH_3 sample. Rearrangement and annihilation of dislocations within the martensite grains could occur during the continuous heating to 600 °C, which affects the accumulation of low-angle grain boundaries and the dislocation density.[56] Furthermore, it seems that future

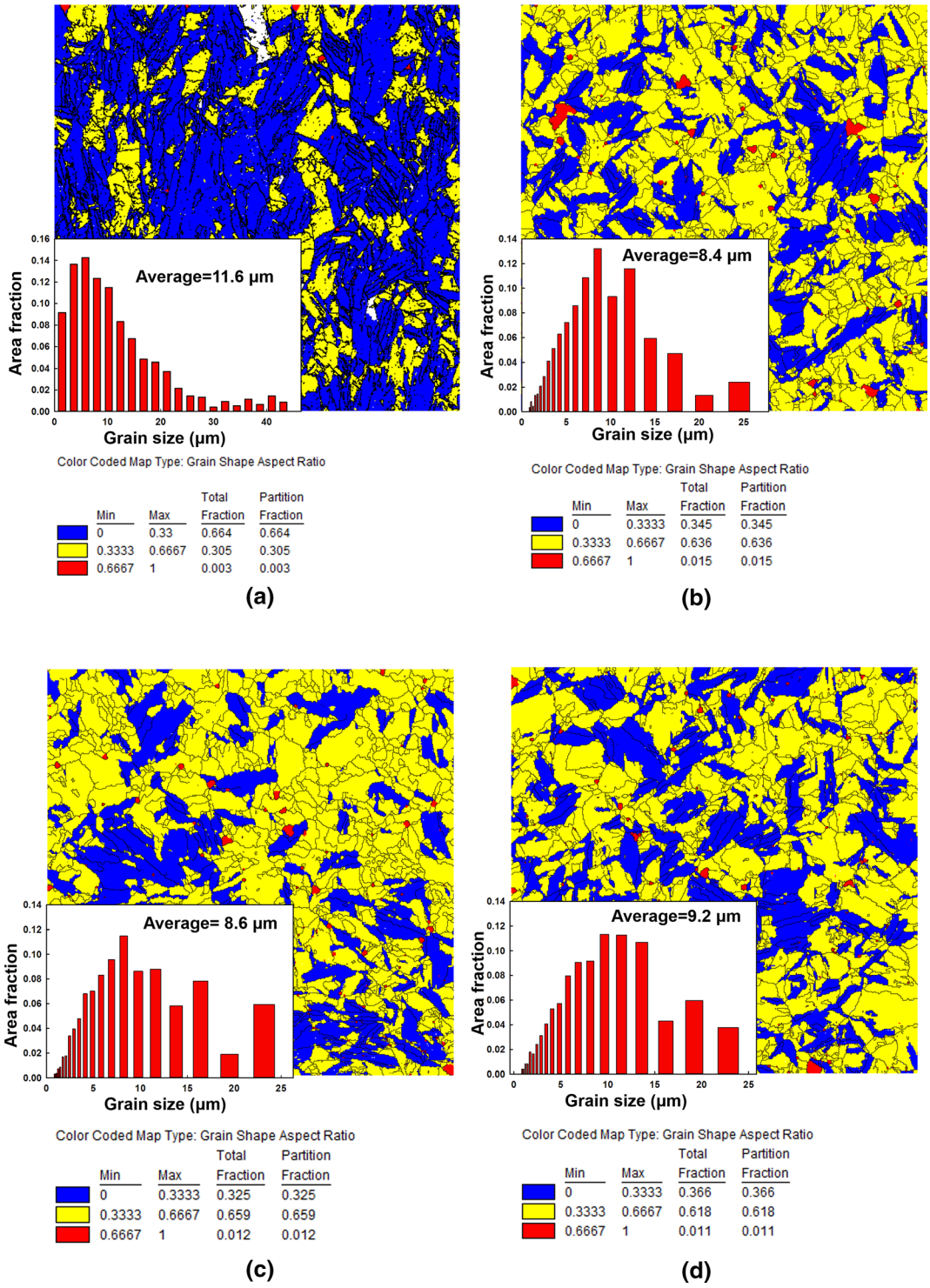

Fig. 9—Grains shaped aspect ratio and corresponded grain size of martensitic structures using 15 deg boundary misorientation to identify the grains of (*a*) A-S_1, (*b*) CH_1, (*c*) CH_2, (*d*) CH_3 samples.

annihilation of dislocations occurred to some extent during the first step of $\alpha' \rightarrow \gamma$ transformation for the CH_2, which are continuously heated to a higher temperature than that of the CH_1.

D. *Microstructure Changes During the Isothermal Heating*

Figures 11(a) through (e) show the inverse pole figure (Z-IPF) maps of the microstructure of the

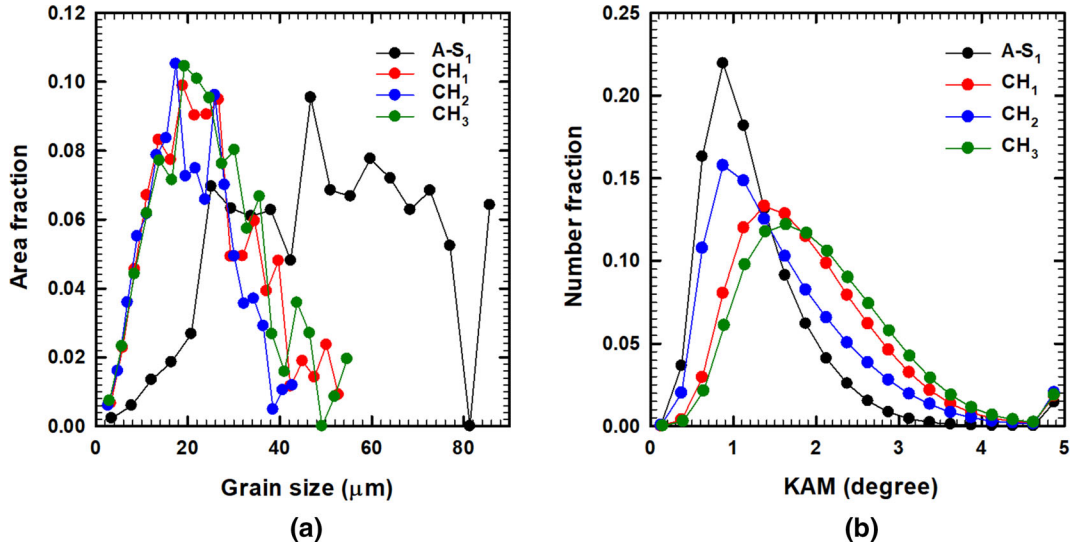

Fig. 10—(*a*) Grain size distribution map of reconstructed PAGs of as-built and continuously heat-treated samples, and (*b*) KAM distributions in martensite of as-built and continuously heat-treated specimens.

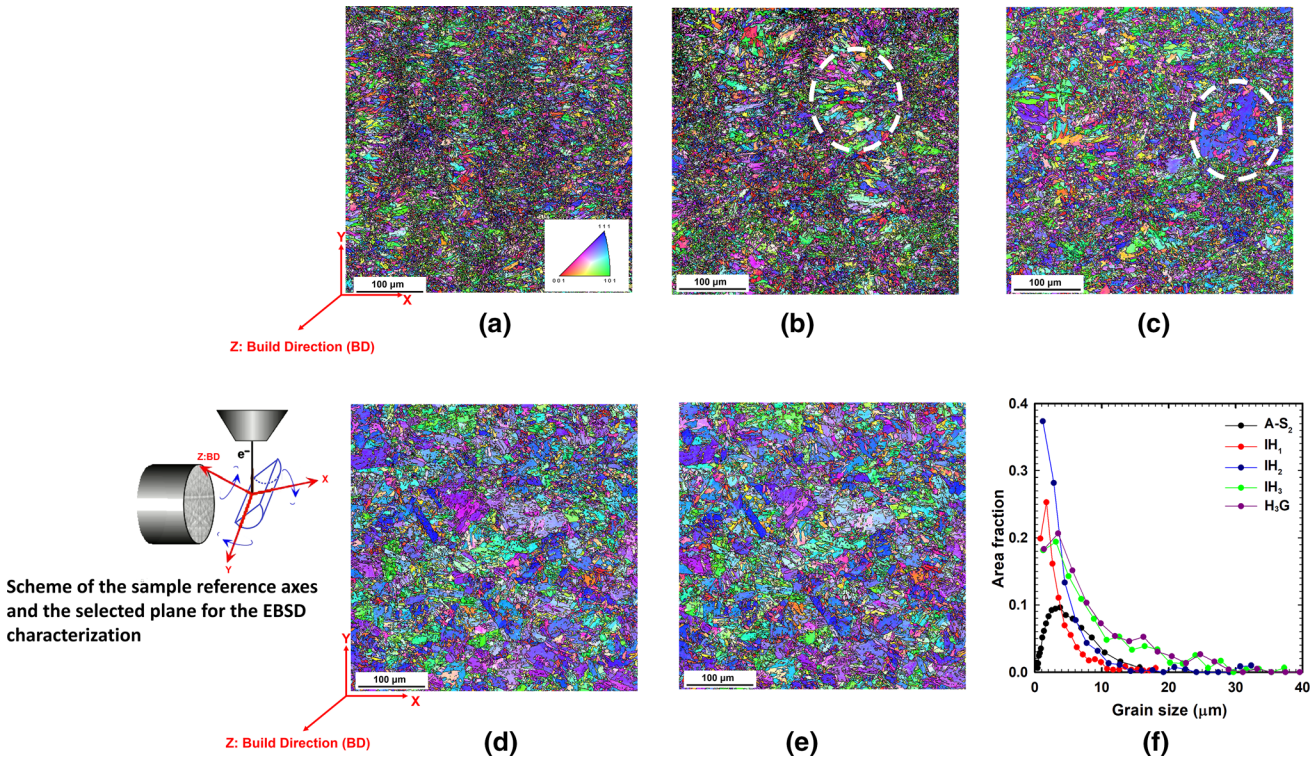

Fig. 11—EBSD analysis of intercritical heat-treated samples, Z-IPF maps of (*a*) as-built sample (A-S_2), (*b*) IH_1, (*c*) IH_2, (*d*) IH_3, and (*e*) H_3G; (*f*) grain size distribution plots.

L-PBF SS CX samples before and after isothermal heating for different periods at 900 °C, which is well above the Af_1 temperature of SS CX alloy, followed by water quenching. The initial microstructure related to the as-built sample is shown in Figure 11(a) for purpose of comparison. With an increase in holding time (Figures 11(b) and (c)), areas of relatively coarse martensite blocks (marked with white dashed circles) are observed, and by further holding up to 60 minutes, the fraction of the coarse martensite blocks seems to increase (Figure 11(d)).

It is observed that the fine martensite structure observed in the as-built sample is relatively replaced by a coarse martensite structure in such grains after 60 minutes of holding at 900 °C. Also, the H_3G sample (Figure 11(e)) indicates an identical microstructure to the IH_3 specimen. Furthermore, the corresponding grain size distribution plots (Figure 11(f)) confirmed that a

significant shift had occurred of the mean peaks of the grain size distribution plots to higher values for the IH_3 and H_3G samples. The average grain size of the IH_3 and H_3G samples is about 8.2 μm and 8.7 μm respectively, which is much higher than that of the A-S_2 (average grain size ~3.9 μm). Although the value of the average grain sizes for the IH_1 (~ 3.4 μm) and IH_2 (~4.1 μm) is close to that of the initial one (A-S_2 sample), some coarser blocks were observed in the martensite structures, which seem to have formed during the isothermal heating process.

E. *TEM Investigations*

Figure 12 shows TEM images taken from the as-built sample (A-S_1) and the continuously heated samples, including CH_1, CH_2, and CH_3, in which isochronal heating at 0.5 °C/s was interrupted at 600 °C, 800 °C, and 1100 °C, respectively.

Figures 12(a) through (d): (I) and (II)) illustrate the bright-field TEM images of the martensitic laths as the dominant phase in all samples, however small darker grains with an elliptic shape are located on PAGs boundaries or triple points in some of the continuously heated samples. Dark-field TEM images (Figures 12(a) through (d) (III) taken from the same area shown in bright-field TEM images using one of the bright spots related to the austenite phase shown in CEBD diffraction patterns (Figures 12(a) through (d): (IV)) confirmed the elliptically shaped grains are associated with the austenite phase in CH_1 and CH_2 samples as well as the dark segregated shape area which is shown in the as-built sample with the red circle. CH_3 sample, which was heated to 1100 °C did not show any trace of the

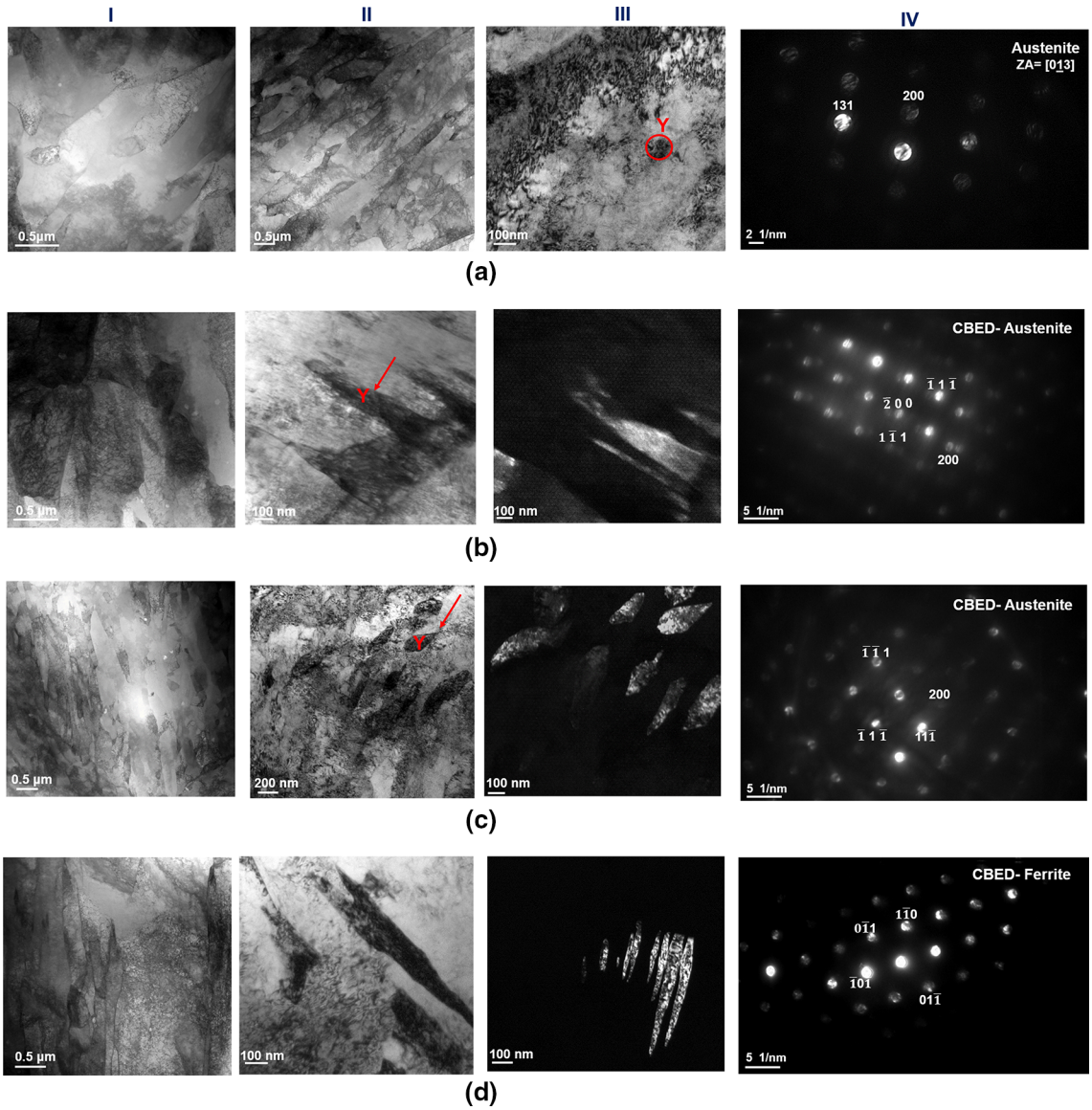

Fig. 12—TEM image of the as-built and continuously heat-treated samples: (*a*) A-S_1, (*b*) CH_1, (*c*) CH_2, and (*d*) CH_3, I: Bright-field TEM images, (II) Bright-field TEM images with higher magnifications, (III) Dark-field TEM images, and (IV) The corresponding CBED diffraction patterns to dark-filed images shown in (III).

austenite as seen in Figure 12(d): (I)-(IV). The austenite visible in Figure 12(b): (II) is located between the lath grain boundaries, whereas the austenite grains detected in CH_2 sample are either located between the lath grain boundaries or are spread to interior of the laths (Figure 12(c): (II)). Also, the TEM observations and the XRD results showed that, in the as-built and CH_3 condition, the alloy contains almost a negligible amount of retained austenite. Thus, the entire austenite detected in the continuously heated samples to 600 °C and 800 °C can be related to reverted austenite. In addition, a comparison between the bright-field TEM images shown in Figures 12(a) through (d): (I) implies the accumulation of dislocations increases for the consciously heated samples compared with the as-built sample. These observations are in agreement with the results obtained of the KAM results shown in Figure 10(b), in which the as-built sample showed the lower KAM value.

To have a clearer observation of the different features formed in the CH_1 sample, higher magnification dark-field TEM images with the EDS maps of alloying elements are shown in Figure 13. The corresponding dark field image (Figure 13(a)) taken from one of the dim spots (Point B) related to the β-NiAl phase in the diffraction pattern (inset in Figure 13(a)) obviously indicates a high number density of fine β-NiAl precipitates in the matrix. The bright field-STEM image in Figure 13(b) with the corresponded EDS maps shows Al and Ni's segregations. It seems that tiny dark points observed from the bright field -STEM image are these segregations. Postulation is the formation of the austenite, and the β-NiAl precipitates simultaneously occurred within the continuous heating to 600 °C. Furthermore, it is stated that the precipitation reactions and the formation of reverted austenite could occur independent of each other.[40]

Corresponding STEM data from the CH_2 and CH_3 samples are shown in Figure 14. Figure 14(a) is a bright field -STEM image and a set of relevant EDS maps from the CH_2 sample. Some dark areas marked by yellow arrows in bright field images of Figure 14(a) are attributed to dislocations. The EDS maps of the CH_2 sample (Figure 14(a)) show zones similar to segregations of Cr and Ni entangled in dislocations. These zones formed probably due to the tunneling effect that occurred in regions closer to zone axes, and this phenomenon leads to more X-ray signal collection. In fact, due to the tunneling effect, more X-ray emission of the specific area could give an impression of segregations in the EDS maps.[57] Moreover, there are no traces of zones similar to segregation areas for the CH_3 sample, as seen in STEM/EDS images in Figure 14(b).

Therefore, it is assumed that heating to higher temperatures of 800 °C and 1100 °C could provide a suitable condition for the diffusion of Ni and Cr, resulting in the formation of homogenous microstructure. Furthermore, no precipitates were found in the CH_2 and CH_3 samples. The TEM/STEM images and corresponding EDS maps from the austenitization annealing—aged sample (H_3G) are shown in Figure 15.

The characterization of the H_3G sample was also chosen to attain information on the mechanism of the austenite reversion at more prolonged times than those related to continuously heated samples. As seen from the bright-filed TEM images, inside martensite laths, a network of dislocation loops exists (Figure 15(a)). Also, traces of Ni- Al precipitations, which can be attributed to NiAl, are detected from Figure 15(b). There are also particles appeared in the EDS maps of Nb, Al, N, and O, enriched in Nb, Al, N, and O. They are probably inclusions and nitride precipitates located immediately adjacent to each other resulting in particle clusters.

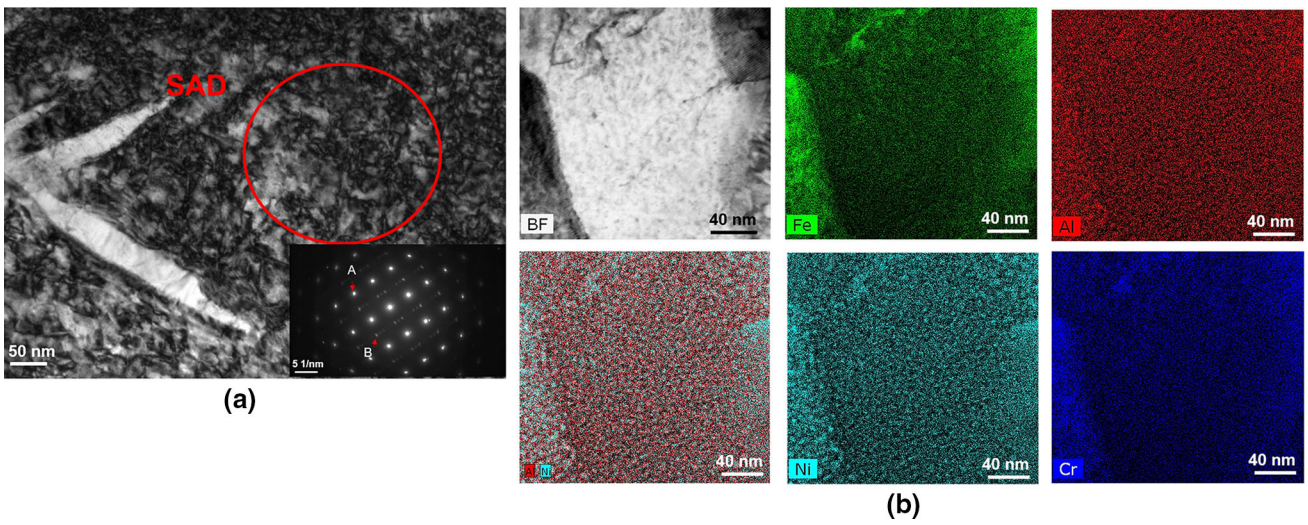

Fig. 13—(*a*) Dark-field TEM image of CH_1 sample with the corresponding electron diffraction pattern from the area marked with the red circle, bright spots are from matrix noted by "A", and dim spots are superlattice spots from precipitates pointed by "B", (*b*) bright field-STEM image with corresponding EDS maps of alloying elements (Color figure online).

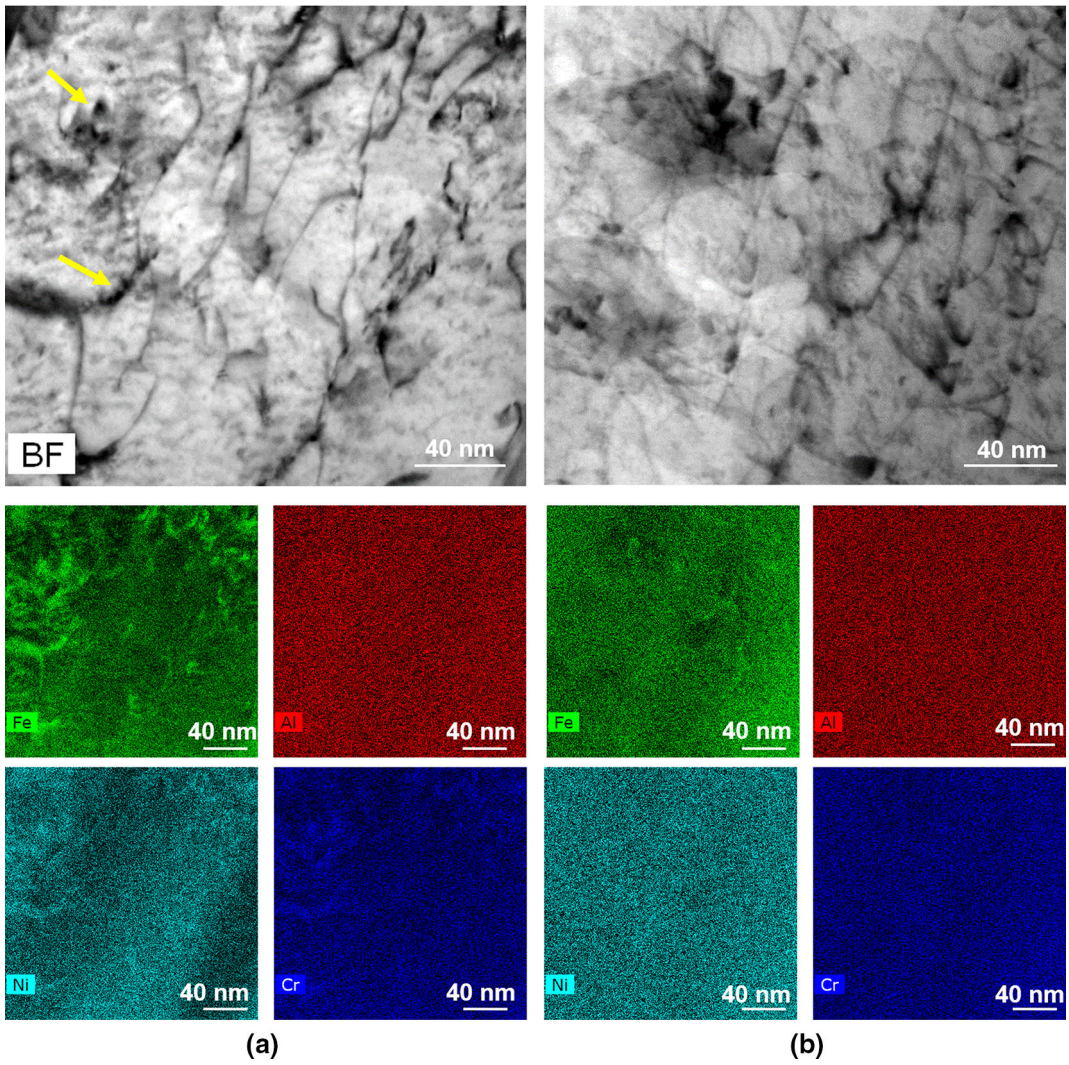

Fig. 14—Bright field -STEM image taken from continuously heated samples with the relevant EDS maps, (*a*) CH_2 sample and (*b*) CH_3 sample.

IV. DISCUSSION

A. *Effect of Heating Rate on Transformation*

The mechanism of phase transformations during continuous heating to three different temperatures and isothermal heating at various soaking times was investigated on the SS CX components. The objective was to gain a better conception of the reverse transformations in this type of parts fabricated by the L-PBF process. The reverse transformation of $\alpha' \rightarrow \gamma$ can occur either by the diffusional process or atomic motion smaller than the interatomic spacing as the shear mechanism, which largely depends on the chemical composition of the steel and the rate of heating employed.[34] Also, it is found that a combination of two or more mechanisms could control the $\alpha' \rightarrow \gamma$ transformation during the continuous heating processes.[58]

As seen from Figure 3(a), the $\alpha' \rightarrow \gamma$ transformation occurred in two steps at heating rates lower than 20 °C/s and with increasing the heating rates to 20 °C/s, the behavior of the two steps $\alpha' \rightarrow \gamma$ transformation changes to a single step transition. Furthermore, both precipitation and $\alpha' \rightarrow \gamma$ transformation begin at higher temperatures as the rate of heating raises and beyond the heating rate of 5 °C/s, no measurable contraction related to the formation of precipitates observed. The appearance of a linear dependency of P_S and As_1 temperatures with rising heating rate shown in Figure 4 could confirm the formation of precipitates and the first step of the $\alpha' \rightarrow \gamma$ transformation occurred through the process of nucleation and growth related to a diffusive mechanism. Although the As_2 temperature did not show a linear dependency with heating rates, a diffusional mechanism of the dissolution and redistribution of the austenite stabilizer elements could control the second step of reversion, which happened at higher temperatures.[59] The observation of the heating rate at 20 °C/s showed that both precipitation and second stage of $\alpha' \rightarrow \gamma$ transformations do not take place and austenite reversion took place in a single step. Therefore, there could be a correlation between the second step of the austenite reversion and the precipitation reaction, in the sense that by eliminating one of them, the other does not

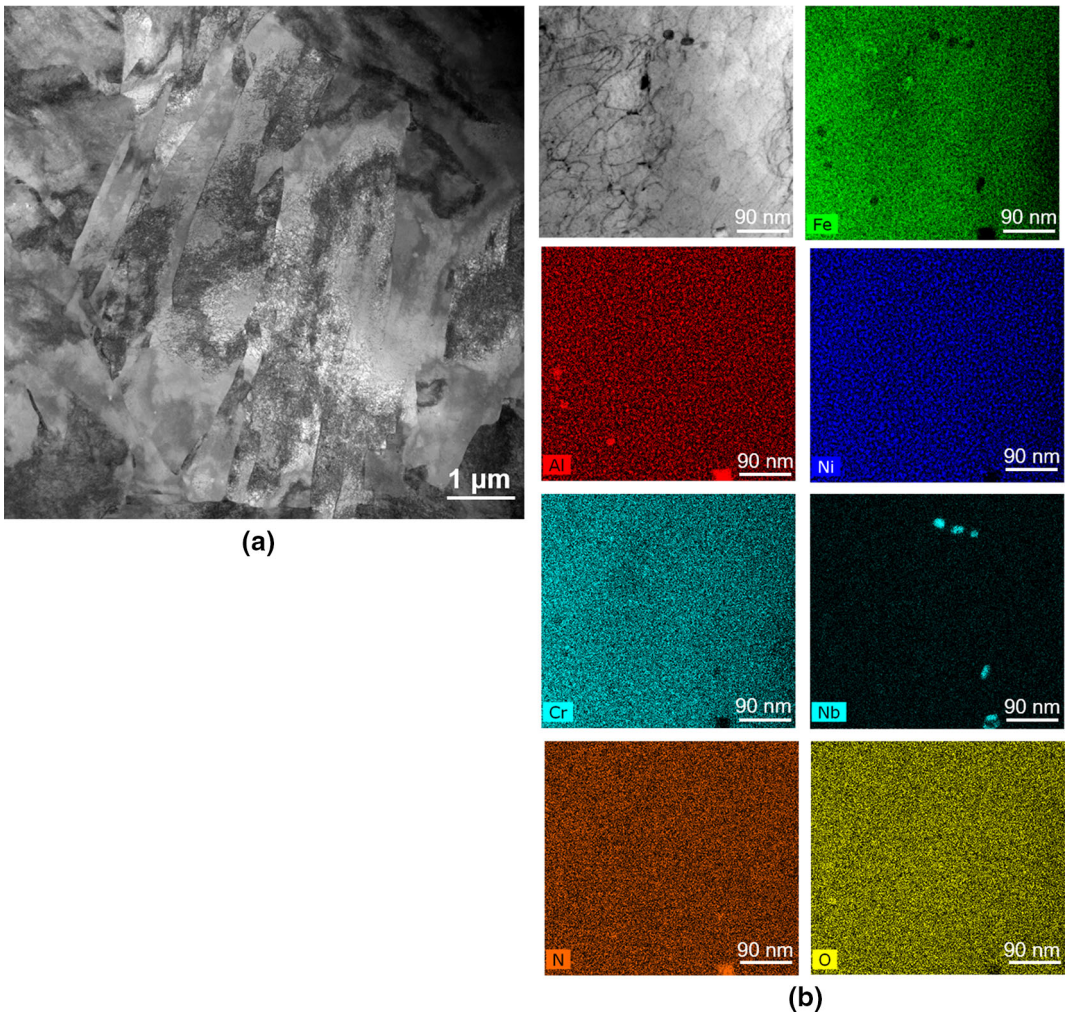

Fig. 15—TEM/STEM images of the austenitization annealing—aged sample (H_3G), (*a*) bright-field image, and (*b*) bright field-STEM image taken from H_3G sample with the relevant EDS maps.

happen. Accordingly, comparing the obtained XRD pattern and the TEM results could help to confirm this assumption.

B. *Austenite Reversion*

According to the XRD results, the continuously heated sample to 800 °C (CH_2) indicated the highest phase fraction of austenite among the continuous heated samples (~5 pct). The heating up to 800 °C ensured that the first step of the $\alpha' \rightarrow \gamma$ transformation and the dissolution of precipitates occurred. Moreover, the TEM/STEM images taken from the CH_2 sample did not show any traces of precipitates, which confirmed that dissolution of precipitates takes place within continuous heating to 800 °C (Figure 14(a)). Thus, the austenite peaks detected from the XRD pattern for the CH_2 sample can be associated with the reverted austenite stabilized by the austenite stabilizing elements obtained from dissolution of β-NiAl precipitates. According to this scenario, the mechanism of the $\alpha' \rightarrow \gamma$ transformation in the first step could be associated with the diffusion of Ni in the martensitic matrix. On slow heating, β-NiAl precipitates are the first features that form and leave depleted zones of Ni their around. One continues heating, the intact martensite far from these precipitates can transform to austenite, which is accompanied by Ni partitioning at a rate controlled by Ni redistribution in martensite. Therefore, the austenite reversion in the first step will depend on the diffusion rate of Ni in the bcc martensitic matrix.[60] The dissolution of β-NiAl precipitates inside martensite tends to happen after, or late in, the first step of austenite formation. The beginning of the dissolution of β-NiAl provides the enrichment zones of Ni, which induce the formation of austenite during the second stage. The presence of reverted austenite does not reveal from the XRD results and the STEM/TEM images related to the CH_3 sample continuously heated to 1100 °C. Also, the second step of $\alpha' \rightarrow \gamma$ transformation was completed at 1100 °C according to the dilatometry curves (Figure 3). By these results, it can be stated that homogenization of Ni as the main austenite stabilizing element, occurs during the heating to 1100 °C. In other words, the localized enriched Ni in the matrix produced

due to dissolution of NiAl following the first step of $\alpha' \rightarrow \gamma$ transformation, as well as Ni concentration gradient within austenite grains of the first step, is homogenized during the second stage and supplies solutes to the martensite-austenite interfaces.[57,61] Therefore, the second stage of transformation could be governed by the diffusion of Ni in the FCC lattice at higher temperatures. Figure 16 indicates a scheme of austenite reversion in two-steps.

The formation and growth of the austenite within the first step of the $\alpha' \rightarrow \gamma$ transformation (Figure 16(a)) associates with the partitioning of Ni between martensite and depends on diffusion of Ni in the martensitic matrix. Also, the diffusion coefficient of Al is higher than that of Ni, which could diffuse to precipitates inside the martensitic matrix. The second step is controlled by the homogenization (redistribution) of Ni profile in austenite behind the martensite-austenite interface and the diffusion rate of Ni in austenite determines the rate of the second step (Figure 16(b)).

The role of time in the reversion process is also evaluated to achieve more insights. Based on the TEM observations, evidence of β-NiAl was also detected for the H_3G sample aged at 530 °C for 3 hours after austenization annealing process. Furthermore, according to the XRD results, the phase fraction of austenite was estimated about 4 pct in this sample. Like the H_3G sample, the presence of β-NiAl precipitates and small elliptic-shaped austenite grains is confirmed from the TEM/STEM micrographs taken from the CH_1 sample. The formation of NiAl precipitates and reverted austenite is also anticipated to occur at the beginning of aging according to the equilibrium calculation of phase fraction by JMatPro shown in Figure 6. Thus, these results assume that the precipitate reaction and the formation of reverted austenite could take place independent of each other. In other words, the nucleation of austenite grains and NiAl particles is thermodynamically possible in the martensitic matrix. From this concept, the initial driving force for the nucleation of reverted austenite does not depend on the dissolution of precipitates.

The XRD results related to the H_3G sample indicated that the phase fraction of austenite in this sample is lower than the value of austenite phase fraction calculated at 530 °C in an equilibrium condition (Figure 6). Therefore, it could be assumed that a diffusional mechanism control further growth of the reverted austenite in the H_3G sample. In other words, the dissolution of precipitates after enough long time of aging provides the suitable condition in which growth of reverted austenite continues by the diffusion of Ni stemming from the dissolved precipitates.[40]

To understand the austenite reversion mechanism, it is also important to evaluate changes in size, shape and orientation of initial parent austenite and reversely formed austenite. The governing mechanism on the $\alpha' \rightarrow \gamma$ transformation determines the shape, size, and orientation of initial prior and reversed austenite during the successive $\gamma \rightarrow \alpha' \rightarrow \gamma$ transformation. Diffusionless shear transformation and the diffusional mechanism with restriction of variant between laths of martensite and reversed austenite can reproduce the same shape, size, and orientations of initial prior austenite in the reverted austenite, which is recognized as the austenite memory effect.[62] Therefore, the absence of preserved microstructural features after the reversion process can correspond to a diffusional mechanism.[21]

In this study, a comparison between the EBSD results of the initial martensitic microstructure ($A\text{-}S_1$) and the continuously heated sample showed that the initial prior austenite of the as-built sample was replaced by smaller and more equiaxed PAGs formed in the continuously heated samples (as shown in Figures 7 and 10). Furthermore, comparing the {001} pole figure taken from reconstructed PAGs of the CH_3 with that of the as-built sample does not exhibit similar ORs (Figure 17), which implies austenite orientation is not preserved, and there is no evidence of the austenite memory effect. A diffusional mechanism could result in the migration of an OR free incoherent interfaces during the austenite

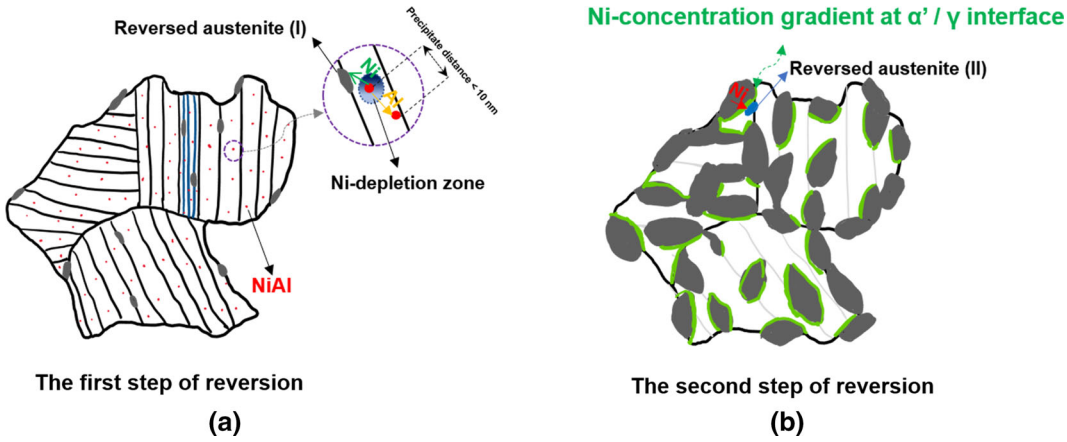

Fig. 16—A scheme of the proposed model for austenite reversion occurred at two stages, (*a*) the first step controlled by Ni-diffusion in the martensitic matrix and affected by the dissolution of NiAl, and (*b*) Ni-redistribution and diffusion in austenite confined nucleation of new austenite at the second stage.

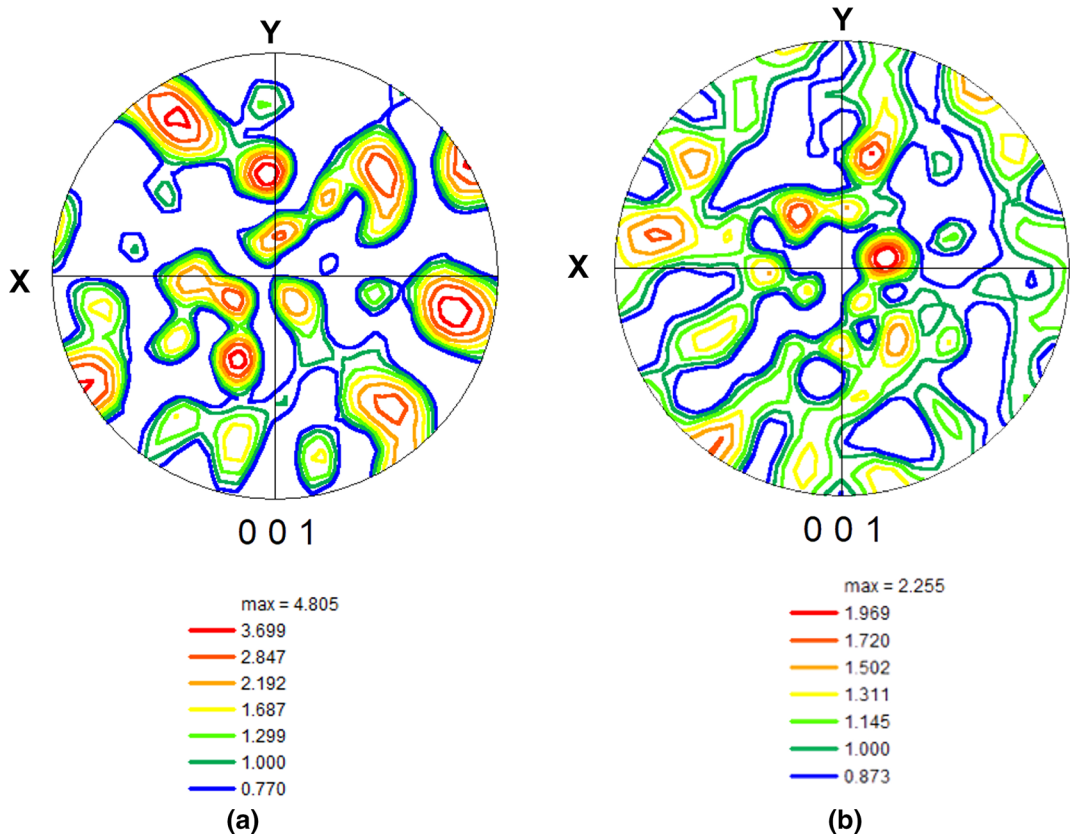

Fig. 17—The {001} pole figure of PAGs corresponded to (*a*) A-S_1 (as-built), and (*b*) CH_3.

reversion upon heating of the initial martensitic structure (as-built). Accordingly, such a difference in OR between the initial PAG and newly reversed austenite formed during the Initial PAG → Martesnite → newly Reversed Austenite → Fresh Martesnite transformation is under a diffusional mechanism,[63] while the martensitic transformation is under migration of a strictly oriented coherent interface.

C. *Recrystallization Following Austenite Reversion*

Research has also been carried out to investigate the possibility of recrystallization and grain growth during the heat-treatment processes. The grain size and the grain shape morphology analyses of continuously heated samples (Figure 9) with the KAM measurements (Figure 10(b)) showed that both grain size and shape of martensitic laths have changed as compared to the initial martensitic microstructure related to A-S_1. The as-built sample shows a hierarchical structure composed of hexagonal cells/sub-grains confined by the bigger micro-grains as shown in Figure 18. These regions could be rich in geometrically necessary dislocations (GND), which provide the required stored energy for initiation of recrystallization during the heating.[64,65] Furthermore, the recovery/recrystallization phenomenon tends to compete with other phase transformations for the stored energy provided from the defects in the structure. Therefore, the phase transformations could suppress or occur concurrently with recovery/recrystallization

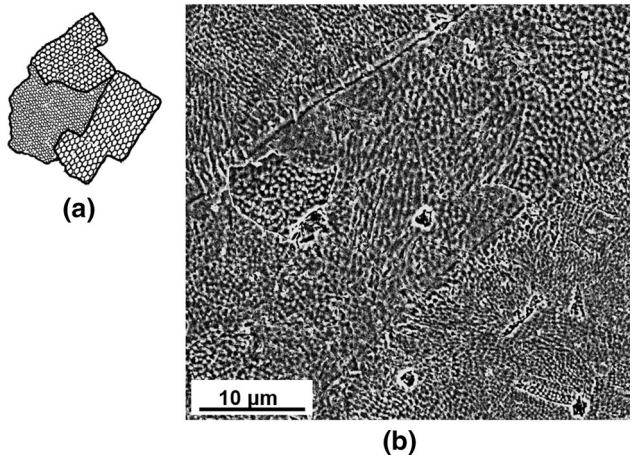

Fig. 18—(*a*) A scheme of a few micro-grains composed of hexagonal cells/sub-grains shown by the black boundaries, (*b*) SEM image showing different micro-grains and sub-grains in the as-built SS CX (A-S_1).

during the competition for consumption of the stored energy.[66] The assumption is that a competition between the partial recovery/recrystallization and reversion of austenite occurring at critical temperatures of $\alpha' \rightarrow \gamma$ transformation within the continuous heating to 1100 °C could change some of microstructural features in the as-built sample (A-S_1). Eventually, this competition could lead to creating a new feature of martensitic

microstructure revealed in CH_3. The larger misorientation angle of the CH_3 sample revealed from the KAM map compared with those of the as-built one can be related to the accumulation of new dislocation during the γ(reverted) $\rightarrow \alpha'$(new) transformation.

Although CH_1 and CH_2 samples similar to CH_3, already experienced competition between recovery/recrystallization and austenite reversion within the pre-treatment (continuously heating to 1100 °C at a heating rate of 0.5 °C/s—soaking for 30 minutes and gas quenching to room temperature), the strain energy produced from the creation of α'/γ interfaces and the volume misfit between austenite to martensite phase change during cooling to room temperature, remained in their new martensitic microstructures.[67] Re-heating to 600 °C and 800 °C could provide activation energy to recovery in new martensitic microstructure resulting in the redistribution and annihilation of point defects and dislocations, either without the formation of new grain boundaries or with the formation and migration of low angle boundaries.[68,69] The relevant KAM map of the CH_1 sample showed a slight shift to lower misorientation angles compared with that of the CH_3 sample indicating partial recovery occurred within the continuous heating to 600 °C. The continuous heating to higher temperatures could also result in a higher tendency to release the stored energy further and finally result in a microstructure with relatively smaller dislocation density.[66] This behavior was also revealed in the CH_2 sample further heated to 800 °C, in which the KAM map displayed a higher shift to lower misorientation angles in comparison with that of the CH_3 sample.

Another type of microstructure evolution is also observed in the isothermally heated samples, contrary to the continuously heated samples. The initial microstructure (Figure 11(a)) is eventually replaced by a more equiaxed and coarser martensitic microstructure (Figure 11(d)). By comparing the initial microstructure (A-S_2) and those of IH_1 and IH_2 shown in Figure 11, traces of slight changes are detectable, which could be attributed to the formation of reversed austenite grains nucleated at high angle grain boundaries (interfaces of initial prior austenite grains). Furthermore, the IH_3 sample showed the initial microstructure is thoroughly replaced by a more equiaxed and coarse grain structure corresponding to the progress of reversion during the longer isothermal holding time. Accordingly, the austenite reversion completed after 60 minutes of holing could imply a long-range diffusional mechanism controlled by Ni's diffusion rate as the main austenite stabilizer element.[70] Moreover, similar to the continuous heating condition, due to the presence of sub-grains and the heterogeneity of grain morphology developed in the as-built structures, there could be a tendency to one or more modes of recrystallization in forms of recovery or recrystallization, which compete with the austenite reversion reaction. Accordingly, the orientation analysis of the isothermally heated samples (Figure 19) indicates that the orientation of the initial martensitic structure (A-S_2 sample) was thoroughly changed after the isothermal heating at 900 °C at different soaking times and the aging process.

Significant differences between the textures developed in the as-built sample and those of isothermally heated samples are related to IH_3 and H_3G samples. The IH_3 and H_3G samples present slightly more preferred {111} ⟨uvw⟩ (ND fiber) texture, which can be associated with the competition of the austenite reversion with recovery/recrystallization.[71,72] Furthermore, the grain size plots of the A-S_2 specimen and those of isothermal heat-treated samples showed the increasing soaking time up to 60 minutes results in a shift of the curves to the right hand, indicating the growth of the nuclei which formed earlier (Figure 11(f)). In summary, Figure 20 schematically illustrates the evolution of possible static recovery/recrystallization and austenite reversion for heat-treated samples.

Recovery/recrystallization and austenite reversion could occur concurrently during the continuous heating and isothermal heating within the as-built microstructure (Figures 20(a) and (b)). The as-built microstructure is composed of micro-grains and sub-grains, which include a high density of dislocations, especially entangled at sub-grain boundaries shown in Figures 20(a) and (b): (I). Accumulation of dislocations and sub-grains results in an increase of the stored energy and consequently leads to a thermodynamically unstable state. For such an unstable state, there is a natural tendency to minimize the stored energy by partial recovery/recrystallization during the continuous heating process (Figure 20(a): II). Furthermore, there is a tendency to nucleation of reversed austenite from grain boundaries at the first step of $\alpha' \rightarrow \gamma$ transformation (Figure 20(a): III). Reaching the temperature of the second stage, the reversed transformation proceeds with formation of a higher fraction of nuclei. The short soaking time of continuous heating also restricted the growth of new austenite grains (Figure 20(a): (IV). Like continuously heated samples, there is a possibility of recovery/recrystallization and austenite reversion within the isothermal heating (Figure 20(b): II). Partial recovery could occur with nucleation of new austenite grains within the initial soaking (Figure 20(b): III), and the phase fraction of austenite nuclei increases with an increase in soaking time (Figure 20(b): IV). Eventually, the austenite nuclei's growth could begin to impinge on another after about 60 minutes of isothermal heating. This phenomenon results in a coarser austenite grain structure than that of the initial PAGs.

V. CONCLUSION

The microstructural evolutions and crystal orientations were studied during the continuous and isothermal heating in SS CX parts fabricated by laser powder bed fusion (L-PBF) technique to understand the reverse transformation mechanism and the possibilities of recrystallization. This study has led to the following findings:

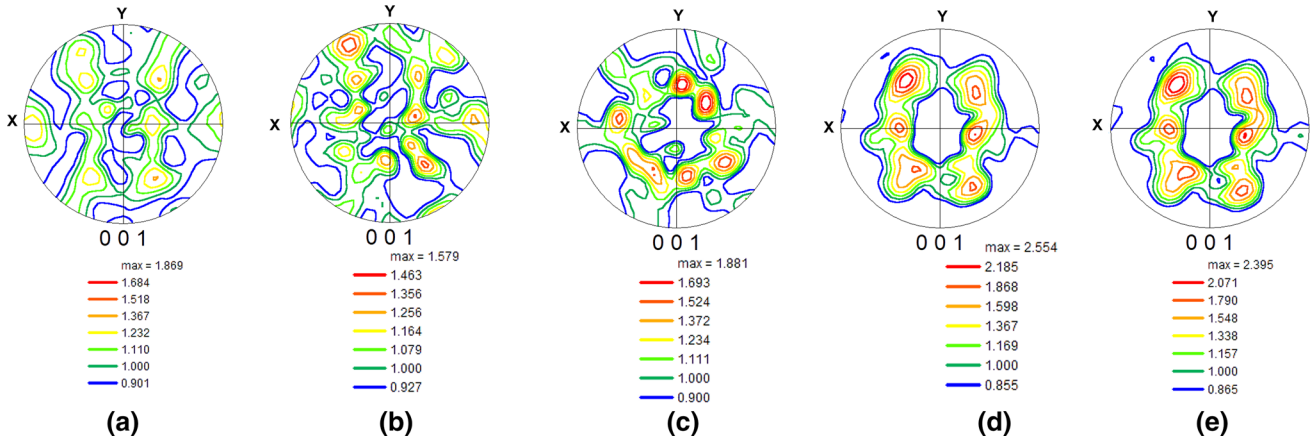

Fig. 19—$\{001\}_{\alpha}$ pole figures of: (*a*) A-S_2, (*b*) IH_1, (*c*) IH_2, (*d*) IH_3, and (*e*) H_3G samples.

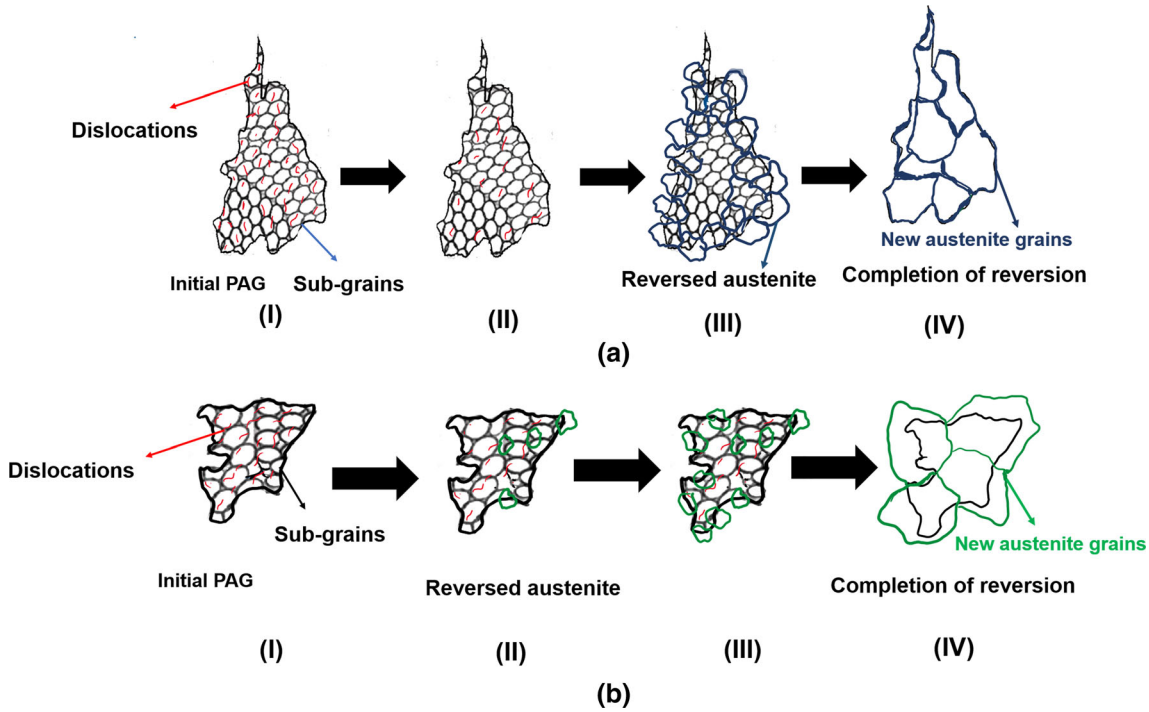

Fig. 20—Schematic illustrations of austenite evolution and possible recovery/recrystallization in (*a*) continuously heated samples: (I): PAG of the as-built sample composed of micro-grains and sub-grains, (II) possibility of a partial recovery/recrystallization within continuous heating, (III): nucleation of austenite grains from sub-grain and PAGs boundaries in competition with recovery/recrystallization, and (IV) completion of the reverse martensite to austenite transformation. Possible recovery/recrystallization and formation of reversed austenite in (*b*) isothermal heat-treated samples: (I) PAG of the as-built sample with micro-grains and sub-grains, (II) initial soaking time: nucleation of new austenite grains with the possibility for the annihilation of accumulated dislocations and consumption of sub-grains, (III): formation of higher fractions of austenite grains after a longer time, (IV): growth of reversed austenite grains with increasing in soaking time to 60 min.

1. The precipitation reactions and two steps of the $\alpha' \rightarrow \gamma$ transformation were observed in the L-PBF SS CX parts during the continuous heating at low heating rates of 0.5 to 5 °C/s. However, the second step of the $\alpha' \rightarrow \gamma$ transformation and the precipitation reaction disappeared from the dilatation curves by a heating rate of 20 °C/s.
2. During the continuous heating at different heating rates, there is a linear dependency between the heating rate and transformation temperatures of the first step of the $\alpha' \rightarrow \gamma$ and the precipitation reactions. Both appears to be controlled by a diffusive mechanism.
3. The collective XRD, TEM and dilatometry observations of the continuously heated samples to 800 °C (double cycles of austenitization) and 1100 °C (single cycle) suggest that the reverted austenite during the first stage forms in the non-depleted Ni zones of martensite away from NiAl precipitates and its growth is controlled by Ni diffusion in martensite. Following the dissolution of NiAl precipitates, the second stage of austenite

reversion proceeds with Ni redistribution in the growing austenite lattice. This homogenization removes the enriched Ni regions due to NiAl dissolution, as well as the concentration gradient of Ni within austenite grains of first stage.

4. The PAGs of the as-built samples were replaced with more equiaxed and finer grains in the continuously heated samples with a difference in OR between the initial PAG and newly reversed austenite structure, which implies the absence of memory effects after completion of reversion.
5. Thermodynamic simulations of NiAl precipitations and reverted austenite observations with the TEM and XRD from the sample continuously heated to 600 °C and the specimen aged at 530 °C for 3 hours, indicated that the reverted austenite nucleates simultaneously and independently from the dissolution of precipitates.
6. The L-PBF process produces heterogeneous hexagonal cells/sub-grains showing micro-segregation and accumulation of dislocations resulting in a thermodynamically unstable state. This heterogeneous microstructure could cause a partial recovery/recrystallization within the subsequent continuous or isothermal heating accompanied by austenite reversion reactions.

ACKNOWLEDGMENTS

Funding provided from Natural Sciences and Engineering Research Council of Canada (NSERC) grant numbers RGPIN-2016-04221 and RGPIN-2017-04368, New Brunswick Innovation Foundation (NBIF) grant number RIF 2018-005, Atlantic Canada Opportunities Agency (ACOA)- Atlantic Innovation Fund (AIF) project number 210414, Mitacs Accelerate Program grant number IT10669 is highly appreciated.

CONFLICT OF INTEREST

The authors declare that they have no conflict of interest.

REFERENCES

1. R. Singh, A. Gupta, O. Tripathi, S. Srivastava, B. Singh, A. Awasthi, S.K. Rajput, P. Sonia, P. Singhal, and K.K. Saxena: *Mater. Today Proc.*, 2020, vol. 26, pp. 3058–70.
2. I. Gibson, D.W. Rosen, and B. Stucker: *Additive Manufacturing Technologies: Rapid Prototyping to Direct Digital Manufacturing*, 1st ed. Springer, Boston, 2010, pp. 36–58.
3. P. Krakhmalev, I. Yadroitsava, G. Fredriksson, and I. Yadroitsev: *Mater. Des.*, 2015, vol. 87, pp. 380–85.
4. T. Niendorf, S. Leuders, A. Riemer, H.A. Richard, T. Tröster, and D. Schwarze: *Metall. Mater. Trans. B.*, 2013, vol. 44B, pp. 794–6.
5. L. Thijs, M.L. MonteroSistiaga, R. Wauthle, Q. Xie, J.P. Kruth, and J. Van Humbeeck: *Acta Mater.*, 2013, vol. 61, pp. 4657–68.
6. K. Kunze, T. Etter, J. Grässlin, and V. Shklover: *Mater. Sci. Eng. A.*, 2015, vol. 620, pp. 213–22.
7. B. Vrancken, L. Thijs, J.P. Kruth, and J. Van Humbeeck: *J. Alloys Compd.*, 2012, vol. 541, pp. 177–85.
8. T. Sercombe, N. Jones, R. Day, and A. Kop: *Rapid Prototyp. J.*, 2008, vol. 14, pp. 300–04.
9. Stainless steel for metal 3D printers| EOS GmbH, (n.d.). https://www.eos.info/en/additive-manufacturing/3d-printing-metal/dmls-metal-materials/stainless-steel. Accessed 19 May 2021.
10. A. Hadadzadeh, A. Shahriari, B.S. Amirkhiz, J. Li, and M. Mohammadi: *Mater. Sci. Eng. A.*, 2020, vol. 787, p. 139470.
11. V.K. Vasudevan, S.J. Kim, and C.M. Wayman: *Metall. Trans. A.*, 1990, vol. 21A, pp. 2655–68.
12. R.J. Hamlin and J.N. DuPont: *Metall. Mater. Trans. A.*, 2017, vol. 48A, pp. 246–64.
13. S. Morito, Y. Adachi, and T. Ohba: *Mater. Trans.*, 2009, vol. 50, pp. 1919–23.
14. C. Cayron, A. Baur, and R. Logé: *Mater. Des.*, 2018, vol. 154, pp. 81–95.
15. N.D. Zemtsova, I.G. Kabanova, and E.I. Anufrieva: *Phys. Met. Metallogr.*, 2008, vol. 105, pp. 19–35.
16. J.M. Pardal, S.S.M. Tavares, M.P. Cindra Fonseca, H.F.G. Abreu, and J.J.M. Silva: *J. Mater. Sci.*, 2006, vol. 41, pp. 2301–07.
17. U.K. Viswanathan, G.K. Dey, and V. Sethumadhavan: *Mater. Sci. Eng. A.*, 2005, vol. 398, pp. 367–72.
18. C. Garcia, L.F. Alvarez, and M. Carsi: *Weld. Int.*, 1992, vol. 6, pp. 612–21.
19. L.F. Alvarez, C. Garcia, and V. Lopez: *ISIJ Int.*, 1994, vol. 34, pp. 516–21.
20. C.A. Apple and G. Krauss: *Acta Metall.*, 1972, vol. 20, pp. 849–56.
21. J. Jeleńkowski: *J. Mater. Process. Technol.*, 1997, vol. 64, pp. 207–14.
22. M. Enomoto and E. Furubayashi: *Trans. JIM.*, 1977, vol. 18, pp. 817–24.
23. C.N. Hsiao, C.S. Chiou, and J.R. Yang: *Mater. Chem. Phys.*, 2002, vol. 74, pp. 134–42.
24. M. Farooque, H. Ayub, A. Ul Haq, and A.Q. Khan: *J. Mater. Sci.*, 1998, vol. 33, pp. 2927–30.
25. P.P. Sinha, D. Sivakumar, N.S. Babu, K.T. Tharian, and A. Natarajan: *Steel Res.*, 1995, vol. 66, pp. 490–94.
26. S.J. Kim and C.M. Wayman: *Mater. Sci. Eng. A.*, 1990, vol. 128, pp. 217–30.
27. M. Sanjari, A. Hadadzadeh, H. Pirgazi, A. Shahriari, B.S. Amirkhiz, L.A.I. Kestens, and M. Mohammadi: *Mater. Sci. Eng. A.*, 2020, vol. 786, pp. 139–365.
28. H. Pirgazi, M. Sanjari, S. Tamimi, B. Shalchi Amirkhiz, L.A.I. Kestens, and M. Mohammadi: *J. Mater. Sci.*, 2021, vol. 56, pp. 844–53.
29. S. Pasebani, M. Ghayoor, S. Badwe, H. Irrinki, and S.V. Atre: *Addit. Manuf.*, 2018, vol. 22, pp. 127–37.
30. S. Cheruvathur, E.A. Lass, and C.E. Campbell: *JOM.*, 2016, vol. 68, pp. 930–42.
31. M. Hunkel, H. Surm, and M. Steinbacher: *Handb. Therm. Anal. Calorim.*, 2018, vol. 6, pp. 103–29.
32. G. Mohapatra, F. Sommer, and E.J. Mittemeijer: *Thermochim. Acta.*, 2007, vol. 453, pp. 31–41.
33. H.K.D.H. Bhadeshia: *Prog. Mater. Sci.*, 1985, vol. 29, pp. 321–86.
34. L. Delaey: Diffusionless Transformations, in: Mater. Sci. Technol, Wiley-VCH Verlag GmbH & Co. KGaA, 2013, pp. 583–654.
35. H. Li, K. Gai, L. He, C. Zhang, H. Cui, and M. Li: *Mater. Des.*, 2016, vol. 92, pp. 731–41.
36. H.S. Yang and H.K.D.H. Bhadeshia: Uncertainties in dilatometric determination of martensite start temperature. *Mater. Sci. Technol.*, 2013, vol. 23, pp. 556–60.
37. B.D. Cullity: Elements of X-Ray Diffraction, 2nd ed., Addison-Wesley Publishing Co, Inc, 1978, pp. 407–17.
38. A. Yadollahi, N. Shamsaei, S.M. Thompson, and D.W. Seely: *Mater. Sci. Eng. A.*, 2015, vol. 644, pp. 171–83.
39. P. Tan, F. Shen, B. Li, K. Zhou: Mater. Des, 2019, vol. 168, pp. 107642.
40. L. Facchini, N. Vicente, I. Lonardelli, E. Magalini, P. Robotti, and M. Alberto: *Adv. Eng. Mater.*, 2010, vol. 12, pp. 184–88.
41. R. Schnitzer, R. Radis, M. Nöhrer, M. Schober, R. Hochfellner, S. Zinner, E. Povoden-Karadeniz, E. Kozeschnik, and H. Leitner: *Mater. Chem. Phys.*, 2010, vol. 122, pp. 138–45.
42. R.A. Abrahams: The Development of High Strength Corrosion Resistant, PhD dissertation, The Pennsylvania State University, 2010.

43. E. Gomes de Araujo, H. Pirgazi, M. Sanjari, M. Mohammadi, and L.A.I. Kestens: *J. Appl. Crystallogr.*, 2021, vol. 54, pp. 569–79.
44. H.L. Wei, J. Mazumder, and T. DebRoy: *Sci. Rep.*, 2015, vol. 5, pp. 1–7.
45. M.A. Valdes-Tabernero, C. Celada-Casero, I. Sabirov, A. Kumar, and R.H. Petrov: *Mater. Charact.*, 2019, vol. 155, p. 109822.
46. S. Suwas and R.K. Ray: *Crystallographic Texture of Materials*, 1st ed. Springer, London, 2014, pp. 73–93.
47. S. Morito, X. Huang, T. Furuhara, T. Maki, and N. Hansen: *Acta Mater.*, 2006, vol. 54, pp. 5323–31.
48. S. Morito, H. Tanaka, R. Konishi, T. Furuhara, and T. Maki: *Acta Mater.*, 2003, vol. 51, pp. 1789–99.
49. H. Kitahara, R. Ueji, N. Tsuji, and Y. Minamino: *Acta Mater.*, 2006, vol. 54, pp. 1279–88.
50. T. Lee, H. Bian, K. Aoyagi, H. Ohnishi, T. Hino, Y. Nakatani, and A. Chiba: Fabricating 9–12 Cr ferritic/martensitic steels using selective electron beam melting. *Mater. Lett.*, 2020, vol. 271, p. 127747.
51. H. Pirgazi, M. Sanjari, S. Tamimi, B. ShalchiAmirkhiz, L.A.I. Kestens, and M. Mohammadi: Texture evolution in selective laser melted maraging stainless steel CX with martensitic transformation. *J. Mater. Sci.*, 2021, vol. 56, pp. 844–53.
52. P. Song, W. Liu, C. Zhang, L. Liu, and Z. Yang: *ISIJ Int.*, 2016, vol. 56, pp. 148–53.
53. X. Zhang, G. Miyamoto, Y. Toji, S. Nambu, T. Koseki, and T. Furuhara: *Acta Mater.*, 2018, vol. 144, pp. 601–12.
54. H. Shirazi, G. Miyamoto, S. Hossein Nedjad, T. Chiba, M. Nili Ahmadabadi, and T. Furuhara: *Acta Mater.*, 2018, vol. 144, pp. 269–80.
55. J.W. Christian: The Theory of Transformations in Metals and Alloys, 1st ed., Pergamon, 2002, pp. 1–1107.
56. F. Niessen, D. Apel, F. Danoix, J. Hald, and M.A.J. Somers: *Mater. Charact.*, 2020, vol. 167, p. 110494.
57. S. J. Pennycook and P. D. Nellist, Eds: Scanning Transmission Electron Microscopy, 1st ed., Springer, New York, 2011, pp. 91–115.
58. R. Kapoor, L. Kumar, and I.S. Batra: *Mater. Sci. Eng. A.*, 2003, vol. 352, pp. 318–24.
59. A. Borgenstam and M. Hillert: *Acta Mater.*, 2000, vol. 48, pp. 2765–75.
60. A. Bojack, L. Zhao, P.F. Morris, and J. Sietsma: *Metall. Mater. Trans. A.*, 2016, vol. 47, pp. 1996–2009.
61. F. Niessen, M. Villa, J. Hald, and M.A.J. Somers: *Mater. Des.*, 2017, vol. 116, pp. 8–15.
62. D. Brandl, M. Lukas, M. Stockinger, S. Ploberger, and G. Ressel: *Mater. Des.*, 2019, vol. 176, pp. 107–841.
63. D.A. Karlyn, J.W. Cahn, M. Cohen: The Massive Transformation in Cu-Zn Alloys, in: Sel. Work. John W. Cahn, Wiley, 2013, pp. 231–235.
64. S. Gao, Z. Hu, M. Duchamp, P.S.S.R. Krishnan, S. Tekumalla, X. Song, and M. Seita: *Acta Mater.*, 2020, vol. 200, pp. 366–77.
65. K. Saeidi: Stainless steels fabricated by laser melting: Scaled-down structural hierarchies and microstructural heterogeneities, PhD dissertation, Stockholm University, 2016.
66. K.K. Alaneme and E.A. Okotete: *J. Sci. Adv. Mater. Devices.*, 2019, vol. 4, pp. 19–33.
67. C. Celada-Casero, J. Sietsma, and M.J. Santofimia: *Mater. Des.*, 2019, vol. 167, pp. 107–625.
68. K. Huang and R.E. Logé: *Mater. Des.*, 2016, vol. 111, pp. 548–74.
69. M. Rout, R. Ranjan, S.K. Pal, and S.B. Singh: *Mater. Sci. Eng. A.*, 2018, vol. 711, pp. 378–88.
70. P.D. Bilmes, M. Solari, and C. Llorente: *Mater. Charact.*, 2001, vol. 46, pp. 285–96.
71. R.H. Petrov, J. Sidor, and L.A.I. Kestens: *Mater*, Trans Tech Publications Ltd, Sci. Forum, 2012, pp. 798–801.
72. R.K. Rayj, J. Jonas, and M.P. Butron Guillen: *ISIJ Int.*, 1994, vol. 34, pp. 927–42.